Probing the southern African lithosphere with magnetotellurics, Part II, linking electrical conductivity, composition and tectono-magmatic evolution.

Sinan Özaydın[1], Kate Selway[2,1], William L. Griffin[1], Max Moorkamp[3]

[1]Macquarie University, ARC Centre of Excellence for Core to Crust Fluid Systems (CCFS), Department of Earth and Environmental Sciences, Sydney, Australia
[2]University of South Australia, Future Industries Institute, Adelaide, Australia
[3]Ludwig-Maximilians-Universität, Department of Earth and Environmental Sciences, Munich, Germany

Key Points:

- Comprehensive comparison of 3D magnetotelluric models and composition from garnet xenocrysts are carried out in southern Africa.
- Depleted regions are associated with resistors, whereas the conductivity of fertile regions depends on the style of metasomatism.
- Kimberlites tend to be around the resistors while avoiding the conductors, suggesting an interplay between mantle composition and magmatism.

Corresponding author: Sinan Özaydın, sinan.ozaydin@protonmail.com

Abstract

The tectonic history of Southern Africa includes Archean formation of cratons, multiple episodes of subduction and rifting and some of the world's most significant magmatic events. These processes left behind a compositional trail that can be observed in xenoliths and measured by geophysical methods. The abundance of kimberlites in southern Africa makes it an ideal place to test and calibrate mantle geophysical interpretations that can then be applied to less well-constrained regions. Magnetotellurics (MT) is a particularly useful tool for understanding tectonic history because electrical conductivity is sensitive to temperature, bulk composition, accessory minerals and rock fabric. We produced three-dimensional MT models of the southern African mantle taken from the SAMTEX MT dataset, mapped the properties of $\sim$ 36000 garnet xenocrysts from Group I kimberlites, and compared the results. We found that depleted regions of the mantle are uniformly associated with high electrical resistivities. The conductivity of fertile regions is more complex and depends on the specific tectonic and metasomatic history of the region, including the compositions of metasomatic fluids or melts and the emplacement of metasomatic minerals. The mantle beneath the $\sim$ 2.05 Ga Bushveld Complex is highly conductive, probably caused by magmas flowing along a lithospheric weakness zone and precipitating interconnected, conductive accessory minerals such as graphite and sulfides. Kimberlites tend to be emplaced near the edges of the cratons where the mantle below 100 km depth is not highly resistive. Kimberlites avoid strong mantle conductors, suggesting a systematic relationship between their emplacement and mantle composition.

Plain Language Summary

The present-day composition of Earth's tectonic plates results from past geological processes. We can learn about Earth's composition from deep rock samples that are carried to the surface during volcanic eruptions and by probing its physical properties, like electrical conductivity, with geophysics. In southern Africa, there are extensive deep rock samples, which have been brought to the surface by kimberlite volcanoes that also host diamonds, and also extensive geophysical data. In this paper, we compare the rock compositions with electrical conductivity to learn more about Earth's composition. Our results show that the oldest parts of the plates that retain compositions similar to their initial composition appear resistive. On the other hand, regions that have been intruded by deep fluids or molten rock can be resistive or conductive, depending on the types of minerals that were formed during the intrusion. The kimberlite volcanoes mostly erupted through the edges of the most resistive parts of the plates and did not erupt through the conductors. These results will help us to make more accurate interpretations about the composition of parts of the Earth where we do not have deep rock samples.

1 Introduction

The Kalahari Craton in southern Africa is an assemblage of Archean and Proterozoic tectonic terranes (De Wit et al., 1992; Jacobs et al., 2008). During three billion years of plate reorganisation, numerous tectono-magmatic events have influenced its compositional structure (e.g., Hanson et al., 2006; Beukes et al., 2019) and are evident not only in surface geology and potential field geophysical data (Corner & Durrheim, 2018) but also in large lateral variations in the state of the mantle inferred from seismic tomography (e.g., Ortiz et al., 2019; White-Gaynor et al., 2020; Fouch et al., 2004; Yang et al., 2008) and magnetotelluric studies (e.g., Evans et al., 2011; Khoza et al., 2013a, 2013b). Due to the presence of extensive outcropping rocks and mantle xenolith-bearing kimberlites (e.g., Griffin et al., 2003; Jelsma et al., 2004), the Kalahari Craton is a great natural laboratory to understand craton formation and survival as well as plate tectonic and magmatic processes throughout geological time. These rocks and xenoliths indicate that

the Kalahari Craton mantle composition is highly variable (e.g., Griffin et al., 2003; Humbert et al., 2019). Variations in mantle composition are either a result of the age-dependent thermal state and composition of the mantle as it initially formed (e.g., Griffin et al., 1999; Pearson et al., 2004) or subsequent alterations imposed by melts and fluids that infiltrated the lithospheric mantle (Alard et al., 2000; Griffin et al., 2003). The Kalahari Craton and its surroundings also hold crucial economic deposits such as the PGE-rich layers of the Bushveld Complex (VanTongeren, 2017) and diamond-bearing kimberlites (Jelsma et al., 2004; A. G. Jones et al., 2009), which formed as the result of lithospheric-scale processes (Begg et al., 2010; Griffin et al., 2013). Therefore, studying lithospheric composition may improve models for economic geology as well as continental evolution.

The magnetotelluric (MT) method is a geophysical technique that images the subsurface electrical conductivity structure of the Earth to upper mantle depths. Electrical conductivity can provide knowledge on bulk composition and temperature as well as the presence of interconnected accessory materials (e.g., fluids, melt, hydrous minerals and sulphides). Previous studies have shown that the cratonic mantle has highly variable electrical conductivity that cannot be accounted for by temperature differences alone (e.g., Selway, 2015; Evans et al., 2011). These conductivity variations can partly be ascribed to hydrogen species structurally bound to the nominally anhydrous minerals (NAMs) that constitute the bulk of the upper mantle, such as olivine, pyroxenes, garnet and spinel (Demouchy & Bolfan-Casanova, 2016).

In this article, we investigate the relationships between the Kalahari Craton's tectonic setting, thermal structure, magmatic events and metasomatic signatures with its geoelectric structure. We use the continental-scale South African Magnetotelluric Experiment (SAMTEX) dataset (A. G. Jones et al., 2009) to produce 3D MT models of the mantle, and we estimate the composition, metasomatic signatures and thermal structure from analyses made on 36066 garnet xenocrysts taken from southern African kimberlites. This article represents the second part of a two-part study. In the first part (Moorkamp et al., 2021), we investigated 3D MT modelling of the SAMTEX dataset using different inversion algorithms (Kelbert et al., 2014; Moorkamp et al., 2011) and aimed to understand the effects of strategies used to model the mantle conductivities. In this paper, we rely mainly on the inversion of the "selected data" dataset run with *ModEM* from a median starting model described in that work, while being mindful of the robustness of these features implied by different modelling attempts. We refer any reader that is interested in the MT modelling aspect of this study to the first part (Moorkamp et al., 2021).

2 Tectonic evolution of the Kalahari Craton and surrounding terranes

The Kalahari Craton consists of terranes with Archean to Neoproterozoic basement ages, namely the Zimbabwe Craton, Kaapvaal Craton, Limpopo Belt, Kheis Belt, Magondi Belt and Rehoboth Terrane (Figure 1). Many of the older basement terranes are hidden under the cover of Neogene Kalahari Group sediments and thick marine-sedimentary sequences of the Jurassic Karoo Group. Due to this cover, most geological understanding of Botswana and the Rehoboth Terrane is derived from geophysical and borehole data (e.g., Chisenga et al., 2020; Corner & Durrheim, 2018). In contrast, the basement rocks of the Kaapvaal and Zimbabwe cratonic nuclei and their immediate surrounding blocks in the eastern Kalahari Craton are better exposed (Figure 1) and have been the subject of rigorous geological and geophysical study for many decades (Oriolo & Becker, 2018; Corner & Durrheim, 2018; De Beer, 2016).

The basement of the Kaapvaal Craton is dominated by 3.6-2.9 Ga gneiss, granitoid and greenstone belts (Poujol et al., 2003). The orientations of the greenstone belts are markedly different in the Kimberley Block in the western Kaapvaal Craton and the Witwatersrand Block in the eastern Kaapvaal Craton, separated by the Colesburg Magnetic Lineament (Figure 1), which suggests the independent formation of these Archean

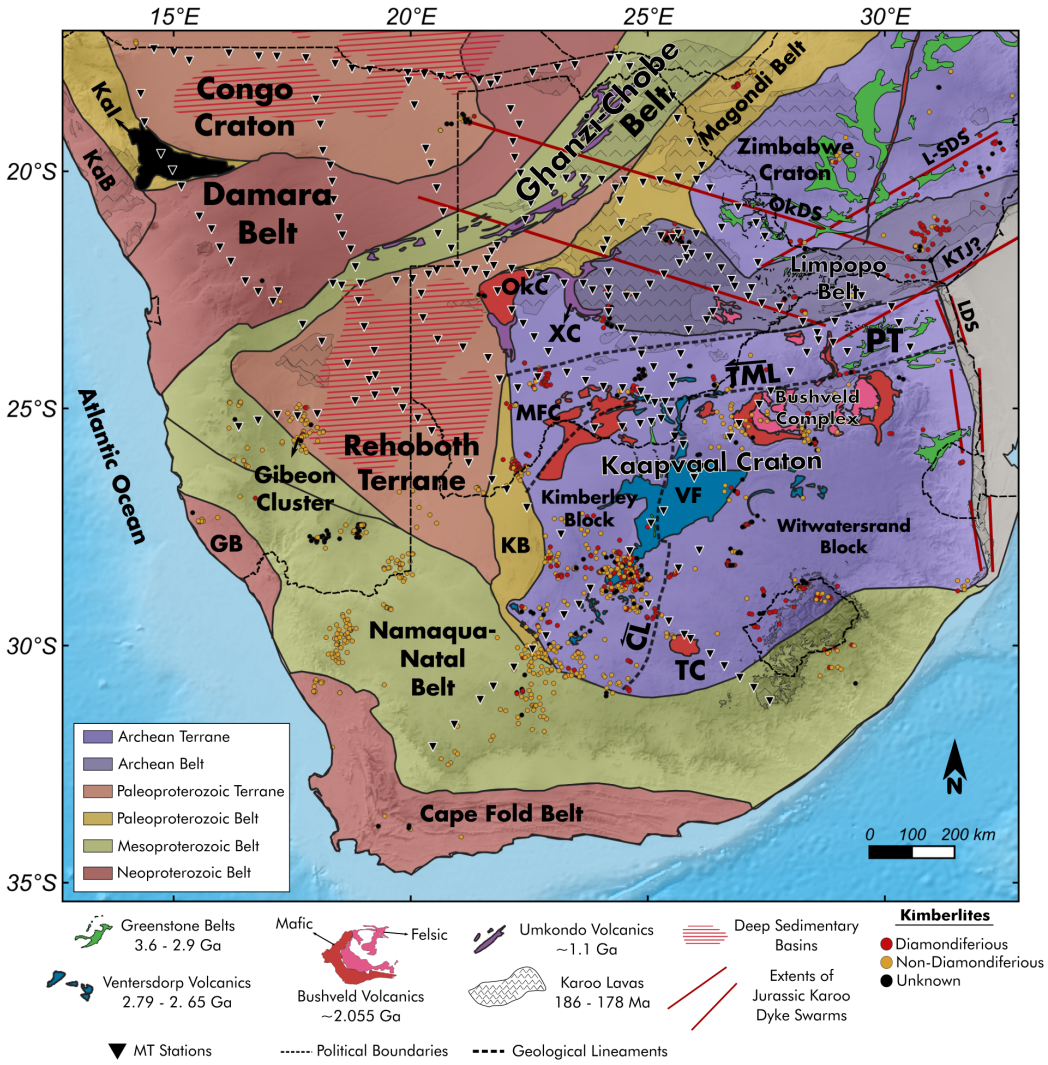

Figure 1. Map featuring the tectonic units of Southern Africa, including greenstone belts and major igneous formations. CL: Colesburg Lineament, GB: Gariep Belt, KB: Kheis Belt, KaB: Kaoka Belt, KaI: Kamanjab Inlier, KTJ: Karoo Triple Junction, LDS: Lebombo Dyke Swarm, L-SDS: Limpopo-Save Dyke Swarm, MFC: Molopo-Farms Complex, OkC: Okwa Complex, OkDS: Okavango Dyke Swarm, PT: Pietersburg Terrane, TC: Trompsburg Complex, TML: Thabazimbi-Murchison Lineament, XC: Xade Complex, VF: Ventersdorp Formation. Data compiled from several studies (McCourt et al., 2013; Hanson, 2003; Corner & Durrheim, 2018; Chisenga et al., 2020)

terranes before amalgamation into a single craton (Jacobs et al., 2008). In the northern Kaapvaal Craton, the Pietersburg Terrane is thought to have accreted to the Witwatersrand Block at 2.73 - 2.65 Ga (Laurent et al., 2019). This collision created the Thabazimbi-Murchison Lineament (TML), a trans-lithospheric structure observed in aeromagnetic data (Good & De Wit, 1997). Assembly of the Kaapvaal Craton was accompanied by the formation of the foreland Witwatersrand Basin (3.0 - 2.78 Ga), the rift-related Ventersdorp Volcanic Sequence (2.79 - 2.65 Ga, Gumsley et al., 2020) and deposition of Transvaal Supergroup (2.6 - 2.058 Ga, Zeh et al., 2020). The final amalgamation of the Pietersburg Terrane with the Witwatersrand Block occurred during the collision between the Kaapvaal Craton and the Zimbabwe Craton to the north. The Limpopo microcontinent was wedged between the two cratons during this collision (2.71-2.67 Ga, Laurent et al., 2019), giving rise to the Limpopo Orogeny and the formation of the Limpopo Belt.

Accretion of the Paleoproterozoic belts and blocks started around 2.06 Ga, corresponding to the timing of the Bushveld and syn-Bushveld magmatism along the TML (Molopo Farms Complex, Okwa Complex, Zeh et al., 2015) and amalgamation of Archean terranes (Laurent et al., 2019; Oriolo & Becker, 2018). The Magondi Belt accreted onto the northwestern end of the Zimbabwe Craton through subduction processes (Master et al., 2010; Jacobs et al., 2008) and then experienced coeval transpressional deformation and metamorphism with the Limpopo Block in response to a collision with an unknown terrane from northwest (Oriolo & Becker, 2018). Contemporaneously, the western end of the Kaapvaal Craton experienced sedimentation of Kheis Belt units and subsequent collision with the Rehoboth Terrane (Jacobs et al., 2008) along the prominent Kalahari Magnetic Lineament (Corner & Durrheim, 2018). The tectonic history and basement geology of the Rehoboth Terrane are somewhat enigmatic due to the thick sedimentary sequences covering the surface, especially in the central region. Geochemical and geochronological data from the westernmost inliers suggest that the Rehoboth Terrane formed and accreted onto the Kaapvaal Craton and Kheis Belt in a convergent-arc setting at 1.77 -1.72 Ga (Van Schijndel et al., 2014).

Following the Paleoproterozoic evolution and cratonisation of the region, by the Mesoproterozoic the assembled Kaapvaal-Limpopo-Zimbabwe-Rehoboth Block was behaving as a rigid block (Jacobs et al., 2008). After stabilisation, the region was impacted by 1.4-1.35 Ga intraplate alkaline magmatism (Pilanesberg Complex and Premier kimberlite Hanson et al., 2006). This was followed by the more abundant and widespread magmatism concentrated near the northwestern border of the craton associated with the $\sim$ 1.1 Ga Umkondo Large Igneous Province, an event thought to be related to rifting (De Kock et al., 2014; Hanson et al., 2006) that used the lithospheric-scale weakness zones formed during assembly of the proto-Kalahari Craton (e.g., Xade Complex, Hanson et al., 2006). The Umkondo-aged rhyolitic units (Kgwebe Formation and southwestern correlatives) mostly outcrop along a ridge in the Ghanzi-Chobe Belt stretching from northeastern Botswana to central Namibia. This ridge was uplifted in response to the Neoproterozoic Pan-African Orogeny, which also formed the Damara Belt (Modie, 2000). To the south, the Kalahari Craton is bounded by the Proterozoic Namaqua-Natal Belt, which formed as an assemblage of numerous microcontinental terranes in a convergent setting. The Namaqua-Natal Belt collided with and accreted onto the Kalahari Craton during series of tectonic events between 1.2 - 1.0 Ga (Jacobs et al., 2008).

The Jurassic breakup of Gondwana had a significant impact on the Kalahari Craton, including the emplacement of widespread rift-related Karoo units (e.g., Drakensberg Lavas, Karoo diorite sills, Okavango and Save-Limpopo Dyke Swarms, Svensen et al., 2012). Following the Karoo event, extensive Group II ($\sim 110-127$ Ma) and Group I ($\sim 110 - 72$ Ma) kimberlites were emplaced in the Kalahari Craton. Differences in mantle xenolith and xenocryst compositions between kimberlites from these two time windows indicate an intervening major metasomatic event in the mantle (Kobussen et al., 2009).

3 Methods

3.1 Garnet xenocryst analyses

Analyses were carried out on existing data collected from 36066 garnet xenocryst samples taken from Group I kimberlites around Southern Africa (Table S1). The data include major-element analyses by electron microprobe and trace-element data collected using with laser-ablation ICPMS techniques, in both the GEMOC ARC National Key Centre, Macquarie University and the DeBeers Group Services Laboratory, Johannesburg, South Africa (Kobussen et al., 2008, 2009). To make depth-dependent classifications, we first performed thermobarometry on these samples. Our methodology in estimating pressure and temperature follows the steps: (1) Calculating P_{Cr}^{max}-T_{Ni} conditions with nickel-in-garnet thermometry and the chromium solubility barometer of Ryan et al. (1996). (2) Fitting a generalized cratonic geotherm of Hasterok & Chapman (2011) based on the locus of maximum P_{Cr} at each T_{Ni}. (3) Defining the temperature at the base of the depleted lithosphere (T_{BDL}) as the temperature at which the proportion of garnets with ≤ 10 ppm (wt) yttrium decreases sharply. (4) Finding the intersection point of the selected conductive geotherm with the T_{BDL} value to obtain the thickness of the depleted lithosphere. (5) Defining the so-called kinked geotherm above T_{BDL} as a line parallel to the diamond-graphite transition (Day, 2012). (6) Finally, projecting the temperatures of garnet samples to the defined geotherm to determine their depth of origin. The calculated geotherm parameters for each pipe are given in Tables S1 and S2, and fitted generalized cratonic geotherm surface heat flow (SHF) values are mapped in Figure 5b.

For the garnet xenocryst classifications depicted in Figures 5 and 6, we used the method of cluster analysis by regressive partitioning (CARP, Griffin et al., 2002). This method classifies Cr-pyrope garnets into statistically significant populations of similar trace- and major-element compositions that define lithology and metasomatic signatures. For the purpose of this work the CARP classes are combined into five main groups: (1) depleted harzburgites, (2) depleted lherzolites, (3) depleted lherzolites with phlogopite metasomatism, (4) fertile lherzolites and (5) melt-metasomatised. Depleted harzburgites and lherzolites (yellow, Figures 5 and 6) represent mantle rocks that have experienced only minor metasomatism since their formation. They are depleted in terms of major- and trace-elements and their garnets show sinuous REE_N patterns (Figure S48-S50), which Griffin et al. (1999) suggested to be a feature related to specific Archean metasomatic processes. Depleted lherzolites with phlogopite metasomatism (blue) have relatively depleted major element compositions but trace-element (Ti, Zr) signatures characteristic of phlogopite crystallisation. The most populous metasomatic class, fertile lherzolites (green), represents rocks with compositions enriched in major and trace elements with more diverse characteristics. These could be rocks that never experienced depletion, or depleted Archean material that was later refertilised. While depleted and refertilised signatures are usually associated with the Archean mantle, signatures of the mantle that has never been depleted are usually associated with Proterozoic or younger mantle (Griffin et al., 2002). Samples from the "melt-metasomatised" class (red) are associated with very enriched, high temperature lherzolites. They commonly show sheared microstructures which indicate melt infiltration into the rock (Griffin et al., 2003) and are largely located below the base of the depleted lithosphere. Whole-rock Al_2O_3 contents used in Figure 5a are calculated from regression analyses made on yttrium-in-garnet (O'Reilly & Griffin, 2006), while $Mg^{ol}\#$ is calculated from the garnet data by the method described in Gaul et al. (2000).

REE_N patterns of the CARP classes mostly demonstrate significantly different characteristics. The sinuosity of the REE patterns is associated with depleted material in the mantle (Griffin et al., 1999) and can be quantified by using the log-Nd_N Dy_N ratio, in which values above zero indicate sinuous patterns and values below zero indicate less sinuous patterns. Yb_N, on the other hand, is used as a proxy of overall HREE enrichment.

Metasomatic CARP classes exhibit less sinuous patterns, heavy REE (HREE) enrichment and light REE (LREE) depletion. During refertilisation, garnet REE_N trends become less sinuous (lower log-Nd_N Dy_N), with higher $HREE_N/LREE_N$ ratios, as the metasomatic fluids percolate more extensively and equilibrate with the environment (Griffin et al., 2003). When the mean values of log-Nd_N Dy_N and Yb_N are plotted against depth (Figure 8b,c), they are correlated (negatively and positively, respectively) with the population of total metasomatic classes within the fertile layer (usually $\sim 100-140$ km). Therefore, we use these parameters as a proxy for the lateral extent of metasomatic fluid percolation in the lithospheric column, or in other words, for the intensity of metasomatism at the corresponding depth.

3.2 Magnetotelluric data and modelling

The MT data used in this study were collected as a tremendous collective effort by the SAMTEX team. Over a decade-long project, the broad-band and long-period stations were set to record at roughly 20-km intervals to investigate the lithospheric architecture of the southern African mantle (A. G. Jones et al., 2009). 3D modelling was not a practical computational possibility at the time of data collection, so the stations are collected in 2D profiles. Most of the data have been published in other studies, utilising some parts of the whole dataset (e.g., Evans et al., 2011; Moorkamp et al., 2019; Khoza et al., 2013a, 2013b; Muller et al., 2009; Miensopust et al., 2011).

The model presented here is produced using the *ModEM* algorithm (Kelbert et al., 2014) for the sparsely selected, good-quality data. The model is designed with 15-km-sized cells at the core of the mesh. Outside the core zone, 8 cells were inserted, increasing in length by a factor of 1.5 to reduce the effects of regularisation. The model consists of 53 cells in the vertical direction. At the shallowest levels, three 50m-thick cells were input to reduce the effects of noise caused by near-surface heterogeneity. Beneath this, 50 cells were inserted starting from a 150m-thick layer with an increasing thickness factor of 1.15. The ocean was added to the model as a fixed resistivity of 0.3 Ωm, with bathymetry from the ETOPO1 global model (Amante & Eakins, 2009). Twenty-five periods between 1-15000 s were chosen for inversion for the sparsely selected, good-quality data. Error floors were chosen as 5% of $\sqrt{Z_{xy}Z_{yx}}$ for all impedance elements.

In the first part of this two-part study (Moorkamp et al., 2021), we explored the effects of MT modelling imposed by data selection, regularisation methods, initial model selection and preference of different modelling algorithms: *ModEM* (Kelbert et al., 2014) and *jif3D* (Moorkamp et al., 2011). Results of this study demonstrated that modelled mantle conductivities could be affected by the regularisation schemes. For instance, *ModEM* tends to converge towards the initial model, whereas the *jif3D* model remains relatively constant as the data sensitivity becomes poorer. To reduce the effects of the regularisation towards the initial model, we chose to apply a more representative initial model in this study. Therefore, the *ModEM* inversion was run from a starting model defined using a long-period median-resistivity filter, which allowed smoothly-varying initial model resistivities across the model. We constructed this initial resistivity model by: (1) Calculating the median determinant resistivity values at periods > 100 s for all stations within 4-degree radius circles centered on each station, (2) assigning that median resistivity value to the station at the center of the circle, (3) making linear interpolations between these values at each station. Outside the interpolation area, $\sim 250\Omega m$ values were used as the median value of all stations at periods > 100 s. The inversion run from this median resistivity half-space had a lower RMS misfit (2.11) than that run from a homogeneous half-space (2.17).

Compositional interpretation of mantle conductivity requires sensitivity tests to be carried out to estimate absolute resistivity values from MT models. We did this by selecting the areas of interest for calculating water contents and other compositional pa-

rameters, replacing the modelled resistivities in these areas with blocks of different resistivity values, and testing the impact on data misfit (Figure S1-S5).

3.3 Methods for determining the links between garnet xenocryst and MT data

Electrical conductivity can be used to infer the composition of the mantle (e.g., Karato & Wang, 2012; Selway et al., 2019). Compositional interpretation can be achieved by integrating experimental conductivity and petrology studies, thermal structure and phase-mixing models (Özaydın & Selway, 2020). Primarily, the electrical conductivity of mantle minerals depends on temperature through semi-conduction processes. Some additional materials such as structurally-bound hydrogen (expressed below as water) can change the thermal energy required to enhance conductivity (e.g., Wang et al., 2006; Dai & Karato, 2014). The extent to which water can be incorporated into mantle minerals is limited (e.g., Férot & Bolfan-Casanova, 2012; Padrón-Navarta & Hermann, 2017) and in some cases the measured mantle conductivities may require an additional conductive phase, either a mineral with a higher activation enthalpy (e.g., phlogopite) or a very conductive mineral with low temperature dependence (e.g., graphite, sulphides Watson et al., 2010; Zhang & Yoshino, 2017).

We used the program MATE (Özaydın & Selway, 2020) to investigate such relationships. For the water calculations, we used the olivine water-partitioning coefficients of Demouchy et al. (2017) and Novella et al. (2014) for pyroxenes and garnet, respectively. We chose to seek solutions of water content up to limits determined by the olivine solubility model of Padrón-Navarta & Hermann (2017) since it reflects the near-pure H_2O state of the cratonic mantle in subsolidus conditions. Water contents were modified for both water-solubility and electrical conductivity models to reflect the calibrations of Withers et al. (2012) for olivine and Bell et al. (1995) for pyroxenes and garnet. Our figures show the water content results using three different olivine conductivity models (Dai & Karato, 2014; Wang et al., 2006; Gardés et al., 2014). Different selections of pyroxene and garnet electrical conductivity models do not make considerable differences (Özaydın et al., 2021). We chose to use the conductivity models of Zhang et al. (2012), Liu et al. (2019), Dai & Karato (2009b) and (Y. Li et al., 2017) for orthopyroxene, clinopyroxene, garnet and phlogopite, respectively. For the mixing model, we used the Modified Archie's model (Glover, 2010). Olivine was set to be a perfectly connected matrix ($m << 1$), while interconnectivity of orthopyroxene was set to $m = 2.5$. Clinopyroxenes and garnet were set to be not connected with a value $m = 4$.

A recent study made detailed comparisons of xenolith water measurements and MT-derived water calculations for the Kimberley-Jagersfontein region (Özaydın et al., 2021) and showed that water contents measured from mantle xenoliths broadly match those interpreted from MT models. Since there are no water content measurements made outside this region in southern Africa, in this work we focus on the trends of the modelled water contents (Figure 7) rather than the specific water contents interpreted from the data.

4 Results

4.1 Lithospheric architecture from magnetotelluric models

MT models produced in this study demonstrate highly variable mantle conductivities across Precambrian terranes with different ages (Figure 3). Archean cratons (Kaapvaal and Zimbabwe cratons) are depicted as complex regions of mostly resistive lithosphere carved by conductive features, reflecting their metasomatic history. In the Kaapvaal Craton (Figure 2a), this is exemplified by the contrast between the conductive mantle beneath the Bushveld Complex and the resistive center of the Kaapvaal Craton (C_1-

C_2, Figure 2a), which appears to have a convex shape very similar to the mantle keels modelled (e.g., Afonso et al., 2008) and imaged by seismic tomography (e.g., Fouch et al., 2004; A. Li & Burke, 2006; Ortiz et al., 2019). North of the Bushveld Complex, at the northern end of the Kaapvaal Craton, the Archean Pietersburg Terrane also appears as a deep resistive feature. Still further north, the Archean Limpopo Belt consists of conductive mantle starting around ~ 50 km depth (LC) and a complex crustal assemblage (Khoza et al., 2013b). The distribution of electrical conductivity in the MT models in this region generally resembles previous 2D models (Evans et al., 2011) and 3D models made in Limpopo Belt (Khoza et al., 2013b), while being modestly different in terms of absolute resistivities and small-scale features in the crust.

One of the MT profiles (Z_1-Z_2, Figure 2h) crosses the Archean Zimbabwe Craton on its proposed southwestern edge. The same profile previously modelled with 2D methods observed a complex crustal assemblage with a thick resistive root beneath the Zimbabwe Craton (Miensopust et al., 2011). These results are similar to ours at the mantle scale, while our model does not exhibit the same complexity in the crust due to larger mesh sizes and restricted frequency selection. Going towards the north, the Magondi Belt is modelled with a moderately conductive lower crust and mantle, bounded to the north by the thick resistive mantle of the Mesoproterozoic Ghanzi-Chobe Belt.

Due to the Neogene Kalahari sediments that cover its surface, the structure of the Archean-Proterozoic Congo Craton is not well known in most places. The craton is a well-defined resistive feature in the westernmost profile near the outcropping Kamanjab Inlier (K_1-K_2, Figure 2b). However, its high resistivity seems to be limited to specific sections within the proposed craton boundaries. Further east (Figure 2c), mantle resistivities become considerably lower in the vicinity of profile B_1-B_2 and then increase to become again more keel-like in the vicinity of profile D_1-D_2 (Figure 2e). A north-south striking conductive feature at lower lithospheric mantle depths beneath the central Congo Craton is hinted at in this model but is more prominent in inversions run with more of the MT stations included (Moorkamp et al., 2021) and is similar to a structure modelled in S- and P-wave tomography studies. Those studies also show that the region surrounding the Kamanjab Inlier has the highest velocities; the lowest velocities are in the central craton and more moderate velocities are modelled near the eastern margin of the craton (White-Gaynor et al., 2020). These results suggest that the Congo Craton, as it is often mapped (Figure 2,3), might be a fragmented tectonic unit and may consist of either a complex tectonic arrangements of blocks of different lithospheric thicknesses or may contain relics of past magmatism beneath its Neogene cover.

The Proterozoic Reheboth Terrane is imaged as a fragmented feature in which the central parts (K_2-K_3, Figure 2b) have a more conductive lower lithosphere (> 100 km), while the northern end nearing the Ghanzi-Chobe region and the Southern Gibeon Fields is modelled with a resistive lithosphere. Similarly, other Proterozoic regions between the Kaapvaal-Zimbabwe-Limpopo Craton and Congo Craton have similar attributes. The youngest of the mobile belts, the Damara Belt, is a Pan-African orogenic zone formed during the collision of the Kalahari and Congo cratons in the late Neoproterozoic and early Cambrian (Goscombe et al., 2017). As imaged by MT models, the Damara Belt consists of a complex crustal assemblage (Khoza et al., 2013a) and a prominent lower crustal and upper mantle conductor (Figure 2c,e,3). Variations in the mantle conductivity of Proterozoic regions suggests that different processes had different effects on the compositional evolution of the mantle.

4.2 Southern African mantle imaged by garnet xenocrysts

A selection of the garnet data from the 100-150 km depth slice is depicted in Figures 4 and 5. The ages of the kimberlite eruptions (Figure 4a) are taken from multiple sources (Supplementary Material, Tables S1 and S2). In situations where the age of the

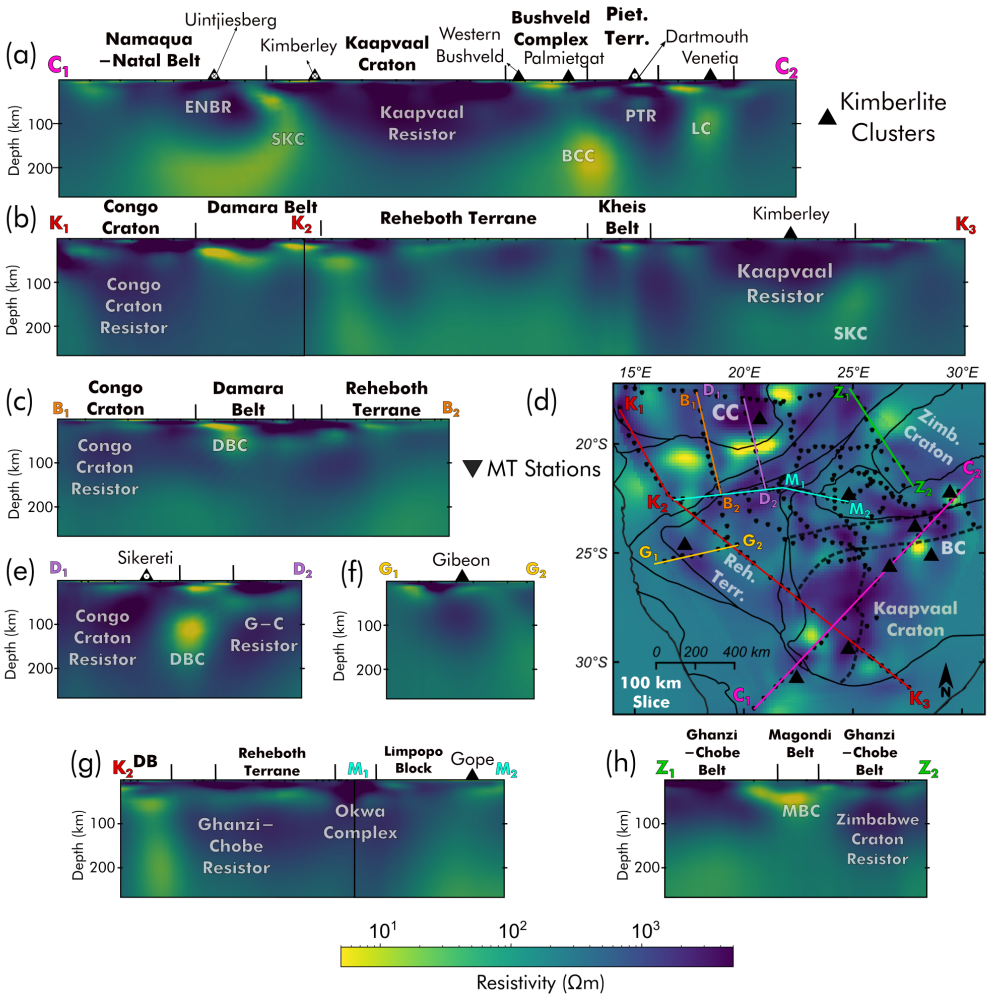

Figure 2. Depiction of the 3D MT model of southern Africa in form of vertical cross-sections (a,b,c,f,g,h). Locations of the cross-sections are indicated in (d). BCC: Bushveld Complex Conductor, CC: Congo Craton, DBC: Damara Belt Conductor, ENBR: Eastern Namaqua-Natal Belt Resistor, G-C: Ghanzi-Chobe, LC: Limpopo Conductor, MBC: Magondi Belt Conductor, SKC: Southern Kaapvaal Conductor, PTR: Pietersburg Terrane

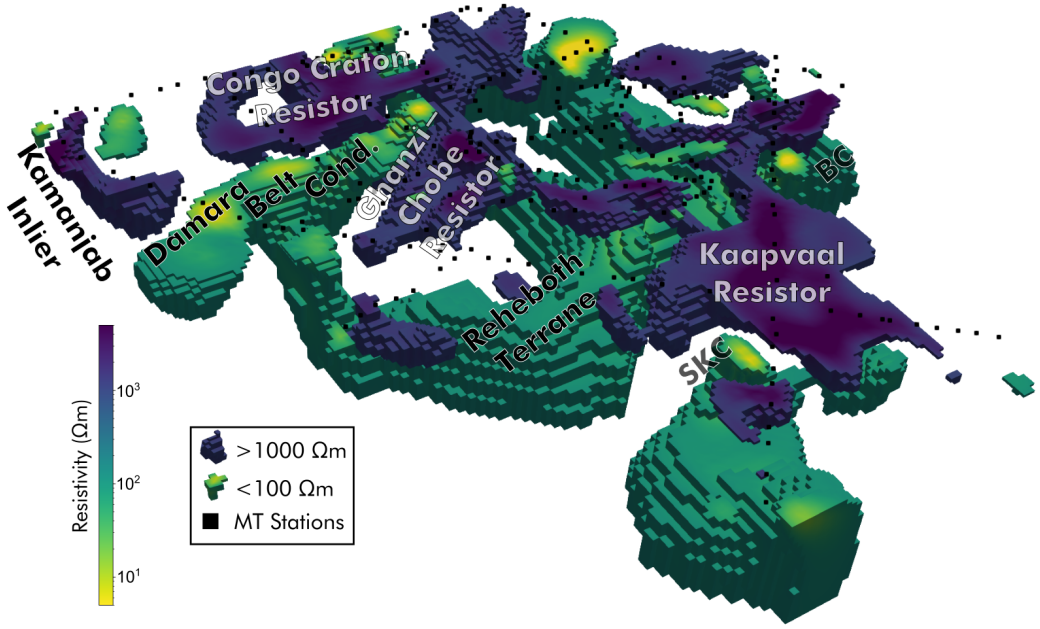

Figure 3. 3D contour plot for values $\leq 1000\,\Omega m$ and $\geq 100\,\Omega m$. BCC: Bushveld Complex Conductor, SKC: Southern Kaapvaal Conductor.

pipe was unknown and the geochemical stratification was very similar to the other pipes within the same cluster, we assumed the kimberlite to be roughly the same age as that cluster. The rest of the unknown ages are represented with black squares. The garnet xenocryst analysis illustrates the complexity of the style of metasomatism in southern Africa and emphasizes that, from region to region, metasomatic fluids had distinct compositions and/or that the initial formation processes of the mantle rocks differed. For instance, iron enrichment (lower $Mg^{ol}\#$) and Al_2O_3 enrichment are not always correlated even though they can both regarded as proxies for the fertility of the mantle (Griffin et al., 2002).

Some generalisations can be made from the existing garnet xenocryst database for Group I kimberlites:

1. Lower whole-rock Al_2O_3, as calculated from Y-in-garnet contents, is a feature of a depleted mantle and mostly appears in Archean regions. On the other hand, higher values point to either a formerly depleted and then refertilised mantle (e.g., Bushveld region) or a mantle that may never have been depleted (e.g., Gibeon).
2. Similarly, higher $Mg^{ol}\#$ values signify higher proportions of depleted material, while lower values of $Mg^{ol}\#$ (< 92) are more indicative of widespread melt metasomatism. In contrast, higher whole-rock Al_2O_3 values are more likely to be related to infiltration of lighter fluids rather than dense and iron-rich melts (Griffin et al., 2003). Therefore, lower values of $Mg^{ol}\#$ usually correlate with a shallower base of the depleted lithosphere, and are more likely to be a feature of the thinner Proterozoic terranes with lithospheric thicknesses between 100-150 km (e.g., Okwa and Uintjiesberg clusters, Figure 6).
3. As expected, the total proportion of metasomatised xenocryst classes is higher in non-Archean terranes. One of the main differences between Archean and Protero-

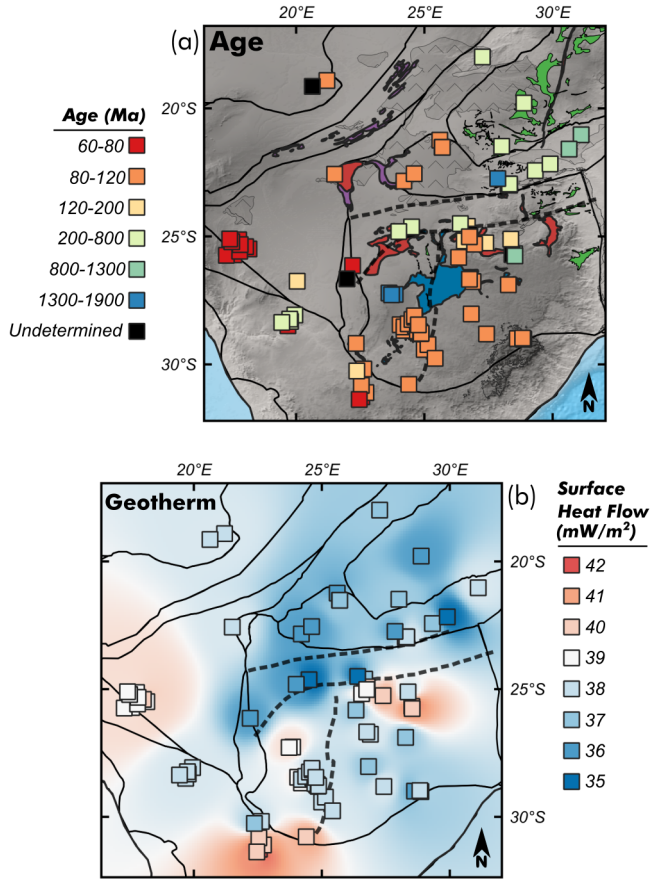

Figure 4. (a) Ages of the kimberlites from which garnet xenocrysts are derived. (b) Surface heat flow value corresponding to the generalised cratonic geotherms of Hasterok & Chapman (2011) as derived from the garnet data.

zoic terranes is the distinct stratification trends observed in Figure 6. Geochemical tomography sections of the Archean mantle usually show a 'depleted layer' between roughly 120-170 km. In contrast, in Proterozoic terranes this depleted material is both less abundant and/or spread throughout the whole depth range in lower proportions.

4. The $CaO-Cr_2O_3$ classification scheme (Grütter et al., 2004) gives a similar story; Archean units are marked by lower proportions of lherzolitic material compared to their Proterozoic counterparts.
5. Ti/Zr can be used as a proxy for phlogopite metasomatism whereby medium to low Ti/Zr ratios generally indicate phlogopite-related metasomatism (Griffin et al., 2002). Very high values of Ti/Zr in some Proterozoic areas (Gibeon, Okwa, Sikereti) might indicate that the fertile material at these locations was not affected by phlogopite-related metasomatism. The pipes with high Ti/Zr ratios mostly plot in the fertile fields on Ti-Zr plots. Most of the xenocryst material from which these fields were originally classified came from garnet lherzolites xenoliths in basalts from off-craton areas and are thought to reflect fertile mantle which never experienced a depletion event. The garnets plotted in fertile fields on Ti/Zr plots are typically a feature of younger mantle (Griffin et al., 2002).
6. 'Unclassified' samples denote garnet analyses that cannot be grouped into the statistically significant types of metasomatism. These garnets most likely reflect the effects of complex metasomatic overprinting, either through multiple episodes by compositionally different fluids. The very high proportions of unclassified garnets observed in the mantle beneath the Bushveld region may indicate such complex metasomatic processes and are associated with a prominent mantle conductor.
7. Figures 5g and h show the mean chondrite-normalised Nd/Dy and Yb ratios of xenocrysts from the different 'Fertile' classes. Garnets with more sinuous REE and HREE-poor characteristics are more abundant near the core of the Kaapvaal Craton (Kimberley and Kuruman clusters), mirroring the amount of depletion observed. The least sinuous and HREE-rich areas appear on the edges of the cratons or areas immediately surrounding them (Uintjiesberg, Jwaneng) indicating the metasomatism in these areas was more extensive.

5 Discussion

If we assume that the connection between composition and electrical conductivity of the mantle can be adequately established through experimental petrology studies, information from garnet xenocrysts and MT models should be compatible. Therefore, we developed interpretations of the southern African lithospheric mantle considering both the broad lithospheric architecture and case by case evaluations of mantle composition. This improves not only our interpretations of MT models, but also of the three-dimensional composition of the southern African lithosphere and our ability to make such interpretations in regions with poorer xenolith constraints.

5.1 Resistivity of Archean, Proterozoic, depleted and metasomatised domains

Electrical conductivity distribution of the Archean terranes varies significantly suggesting that metasomatic events left a compositional mark on the initially depleted lithosphere. Similarly, Proterozoic terranes assembled near the Archean cratons do not show consistent characteristics and architectures that would provide a simple relationship between lithospheric thickness, age and composition from the electrical conductivity distribution. The south-central Rehoboth Terrane, for instance, demonstrates lower resistivities (K_2-K_3, Figure 2b). In contrast, the Gibeon area, which includes one of the clusters of Cretaceous kimberlitic volcanism, is imaged as a highly resistive region. Similarly,

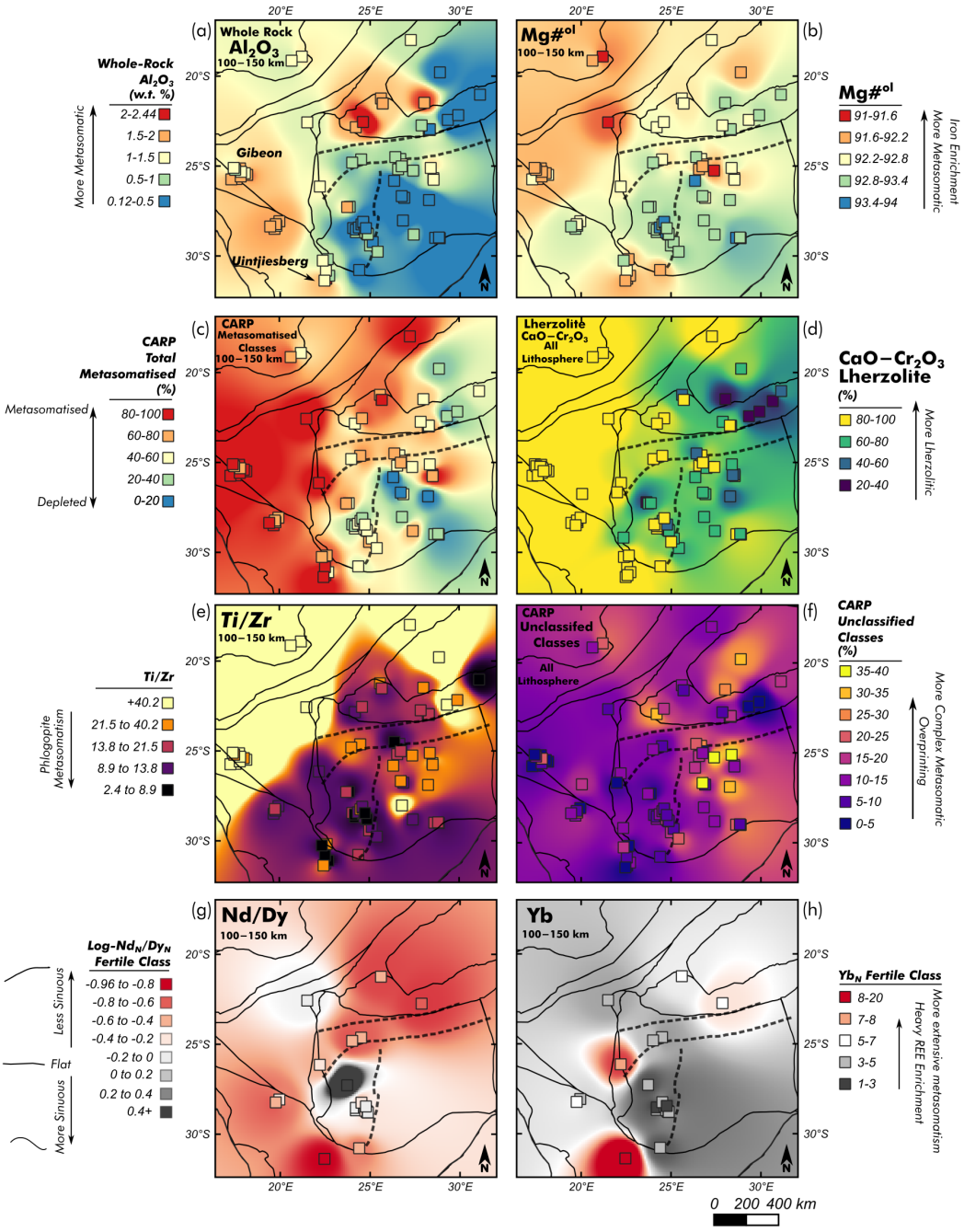

Figure 5. Maps of information derived from garnet xenocrysts. Data only exist at kimberlite localities and all other shading is interpolated with a 4-degree inverse distance weighting method. We excluded data points with fewer than 10 samples for the parameter in question. (a) Whole-rock Al_2O_3 contents derived from Y-in-garnet from 100 to 150 km. (b) $Mg^{ol}\#$ of olivine derived from garnet compositions from 100 to 150 km (c) Total percentage of metasomatic CARP classes: 'Fertile', 'Depleted lherzolite with phlogopite metasomatism' and 'Melt metasomatism'. (d) Percentage of garnets classified as lherzolites from $CaO - Cr_2O_3$ classification. (e) Ti/Zr ratios of garnets, where lower values indicate phlogopite metasomatism. (f) Percentage of samples that do not fit a defined CARP class, likely to indicate more complex overprinting. (g) Chondrite-normalised log-Nd/Dy taken from garnets classed as 'Fertile'. (h) Chondrite-normalised Yb values taken from garnets classed as 'Fertile'.

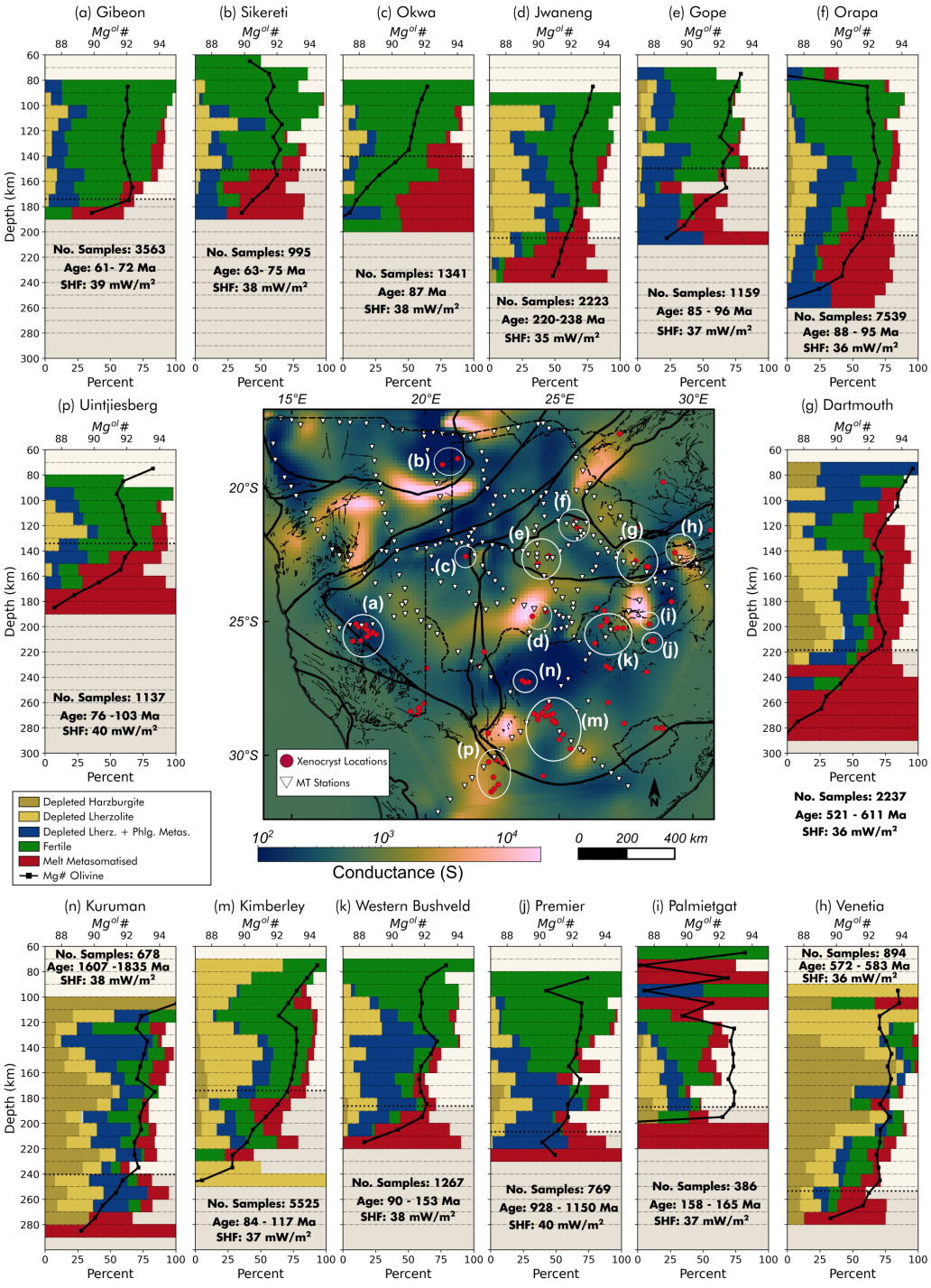

Figure 6. Comparison of CARP sections depicted as 10 km interval histograms and olivine $Mg^{ol}\#$ with modelled mantle conductance (50 - 200 km). Locations of the kimberlite clusters are denoted in the map (a-p). SHF: Surface heat flow value of fitted generalized cratonic geotherm (Hasterok & Chapman, 2011). Horizontal dotted line indicates the base of the depleted lithosphere (BDL).

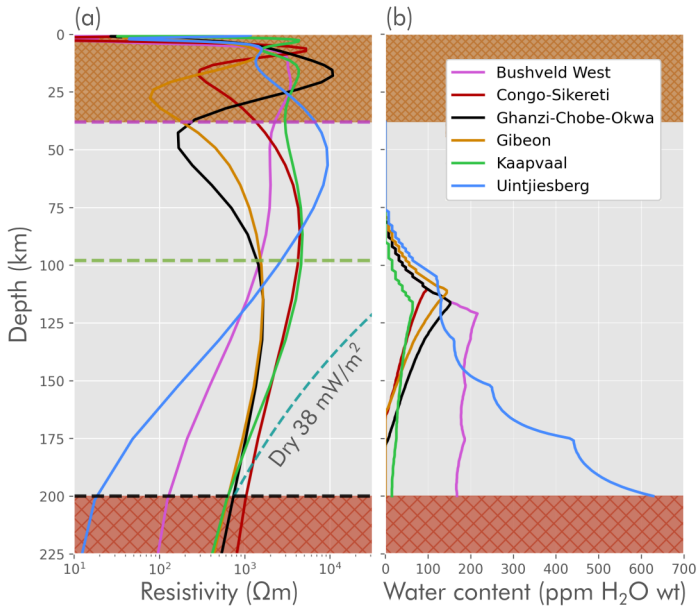

Figure 7. (a) Vertical profiles extracted from the 3D model at the locations of: Bushveld West cluster, Congo Craton (Sikereti cluster), Ghanzi-Chobe Belt (Okwa cluster), Gibeon Fields, Kaapvaal Resistor, Uintjiesberg cluster. (b) Water contents calculated from selected areas from the MT model. Bulk rock water contents are calculated up to the distributed olivine water solubility limit defined by the model of Padrón-Navarta & Hermann (2017) for the selected profiles and the thermal structure derived from the nearest kimberlite clusters. Water contents reported in this figure use the calibrations of Withers et al. (2012) for olivine and Bell et al. (1995) for pyroxenes and garnet.

the northern end of the Rehoboth Terrane and adjacent Ghanzi-Chobe belt possibly shows the greatest depths at which $1000\Omega m$ resistivity is observed (Figure 11b). Such high resistivities have been previously imaged in Proterozoic regions surrounding older cratons (e.g., Selway, 2015; Selway et al., 2011) and their high resistivities have been interpreted as reflecting magmatic and plate tectonic processes that induced mantle melting and depletion. In southern Africa, the resistors around the Ghanzi-Chobe Belt line up with the 1.1 Ga Umkondo magmatic units (Modie, 2000). This area was the focus of rifting and extensive melting during the breakup of the Rodinia Supercontinent (De Kock et al., 2014) which might have created the depleted resistive mantle with low volatile contents that we observe today; similar features are seen in models of the Mozambique Belt, a region of Pan-African aged magmatism and high-grade metamorphism and a currently active rift zone (Selway, 2015). If the relationship between rifting events and volatile extraction from the melting of the mantle can be more confidently linked, the MT models of the Ghanzi-Chobe belt may provide evidence for a rifting origin for the Umkondo magmatism (De Kock et al., 2014).

5.2 Kimberley

The Kimberley domain is rich in xenolith-bearing diamondiferous kimberlites from which we have 5521 garnet xenocrysts to map the lithospheric mantle. Previous studies of garnet xenocrysts have demonstrated that the area was metasomatised by an event that occurred between the eruptions of Group II (120-180 Ma) and Group I (90-120 Ma) kimberlites (Kobussen et al., 2009; Griffin et al., 2003). Group II kimberlites are pop-

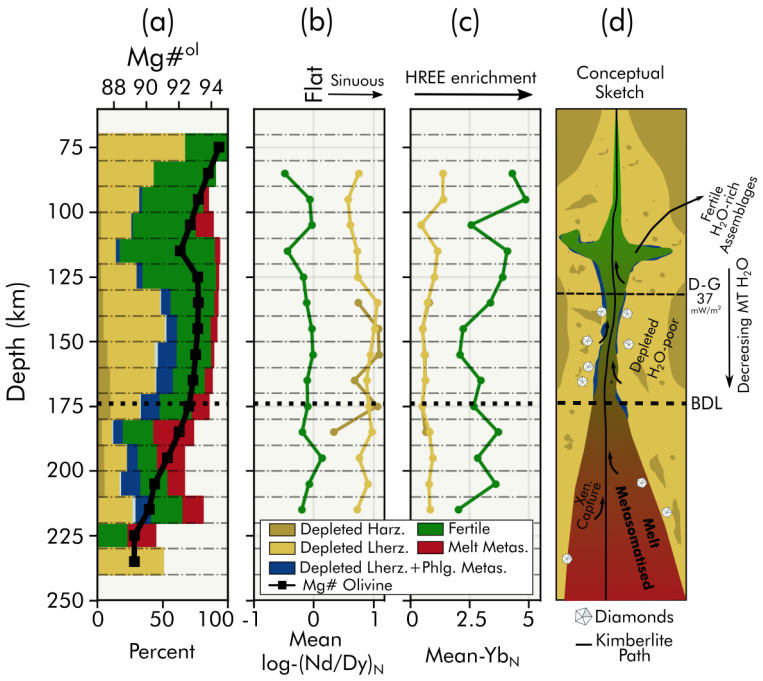

Figure 8. Composition of the Kimberley area deduced from garnet xenocrysts depicted as (a) CARP "geochemical tomography" section with $Mg^{ol}\#$, (b) log - Nd/Dy_N values as a proxy for the sinuosity of garnet REE patterns, (c) Yb_N values as a proxy for HREE enrichment. (d) Conceptual sketch of the interpreted compositional section considering the water content interpretation of Özaydın et al. (2021). D-G: Diamond Graphite transition at 37 mW/m^2 geotherm, BDL: Base of the depleted lithosphere.

ulous in this area, reflecting modal metasomatic modification of the mantle prior to kimberlite emplacement (Giuliani et al., 2015).

The Kimberley-Jagersfontein area is geochemically stratified into three layers: (a) A fertile layer between 90-130 km that is marked by lower $Mg^{ol}\#$ values, (b) a depleted layer between 125-175 km and (c) an underlying melt-metasomatised layer. Our MT results demonstrate that the Kimberley domain overlies a lithosphere with relatively low resistivities (the greatest depth at which 1000 Ωm is modelled is $\sim 100-120$ km, Figure 11b) compared to the main Kaapvaal resistor ($>$ 150 km, Figure 11b). The conductive nature of the lithosphere beneath 100 km might reflect the chemical alteration observed in garnet xenocrysts.

In a recent study, Özaydın et al. (2021) compared garnet xenocrysts, xenolith water contents and MT models in the Kimberley-Jagersfontein region. These analyses demonstrated that water contents calculated from MT models decreased with depth between 100 to 160 km, which roughly agrees with the measured xenolith water contents. However, a larger misfit was observed in the depleted layer, suggesting a local metasomatic control around kimberlite conduits. Since the fertile layer corresponds to a water-saturated zone and calculated water contents can account for observed xenolith water contents, the authors considered the metasomatism in the fertile layer has to be laterally extensive enough to be sensed by electromagnetic fields. In support of this argument, we found that log-Nd/Dy_N and Yb_N values correlate with the number of garnets classified as metasomatised in the fertile layer (Figure 8). Given that increasing metasomatism leads to less sinuous log-Nd/Dy_N patterns and more $HREE$ enrichment in garnet xenocrysts (Griffin

et al., 2002), we suggest that the metasomatic fluids pervasively percolated through the fertile layer, peaking around 110-120 km depth. As a result, the kimberlites sampled more fertile material at this depth.

A conductor bounds the Kimberley region to the east (Figure 2a). Like the Molopo Farms and the Bushveld complexes, this conductor coincides with a large Paleoproterozoic mafic intrusive complex (1.9 Ga, Maier et al., 2003), the Trompsburg Complex (TC, Figure 1). Since it does not have surface exposure, existing knowledge about the complex is limited to gravitational modelling and few borehole measurements (Rezaie et al., 2017). We think the conductor here may be related to the emplacement of the mafic magmas and a metasomatised residue.

5.3 Bushveld magmatic event and its effects on composition of the lithosphere

The Bushveld Complex (BC) is a large igneous body emplaced between 2.055-2.06 Ga, intruding Transvaal Group sediments (Scoates et al., 2021). The complex outcrops as mafic-ultramafic eastern, western and northern lobes (Rustenberg Layered Suite) and slightly younger felsic rocks towards the centre (Figure 9a). A strong stratigraphic and geochemical concordance between the mafic intrusives in the different lobes suggests connectivity between them or a co-genetic relationship (Kruger, 2005). Gravity models of the Bushveld Complex demonstrate that surface exposures of the complex are continuous at depth and define a lopolith structure with a maximum thickness exceeding 8 km (Cole et al., 2014). The Palmietgat kimberlite pipe, near the centre of the Bushveld Complex, contains xenoliths of plagioclase-bearing lower-crustal pyroxenites petrologically akin to the pyroxenites of the Rustenburg Layered Suite, indicating connectivity between the underlying western and eastern lobes (Webb et al., 2011). Zircon U-Pb dating constrains the emplacement of the Rustenberg Layered Suite to a one million year time window, indicating extremely high magma fluxes (Zeh et al., 2015). The lower units of the Rustenberg Layered Suite hold economically valuable, PGE-hosting chromitite layers (e.g., Merensky Reef) that contain more than 80% of global platinum reserves (VanTongeren, 2017). Both the source of the parental magma and the magma chamber differentiation processes necessary to produce such PGE-rich chromitite layers are still debated (Cawthorn, 2015; VanTongeren, 2017). Considering the targeting depths of our MT models, the most relevant ideas to investigate are speculations about the mantle component required in the parental magmas to generate the specific properties observed in the intrusives (Zirakparvar et al., 2014; Richardson & Shirey, 2008).

More than ten adjacent magmatic bodies, each with geochemical affinities to the BC, were emplaced during the same narrow time window (Figure 9a, Rajesh et al., 2013), and generally are considered to be satellite intrusions. One of these satellite magmatic bodies, the Molopo Farms Complex (MFC, Figure 1), is a layered mafic intrusion situated in southern Botswana roughly 400 km west of BC (Beukes et al., 2019). The stratigraphic layering of the MFC is similar to the lower layers of the BC, but available borehole data indicate it lacks the PGE-rich chromitite layers (e.g., Kaavera et al., 2018). The BC and these satellite intrusions may have formed as part of a larger Bushveld Large Igneous Province, which used a structural weakness corridor along the Thabazimbi-Murchison Lineament (TML, Rajesh et al., 2013).

5.3.1 Garnet xenocrysts and composition of the Bushveld mantle

Garnet xenocrysts that sampled the mantle in the vicinity of the BC show more variable geochemical signatures from pipe to pipe, in contrast to those from Proterozoic terranes or those from the Kimberley region. They are concentrated around the BC or close to the limbs of the Rustenberg Layered Suite. Only the Palmietfontein and Palmietgat pipes fall within the boundaries of the complex. Compared to those from the south-

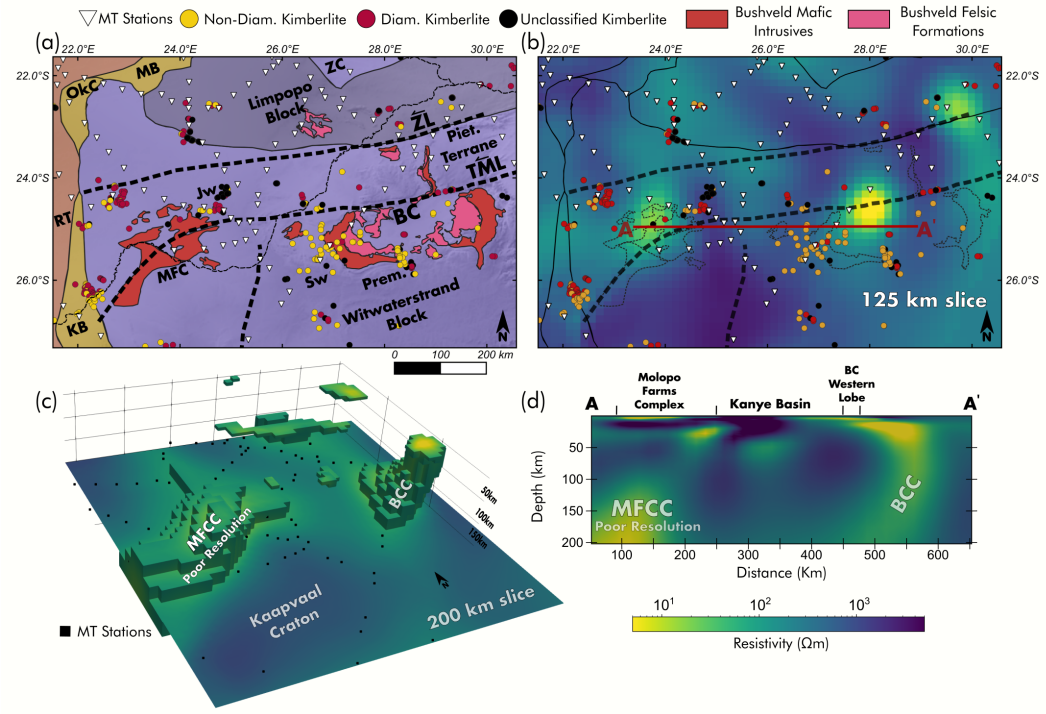

Figure 9. (a) Map of the region containing Bushveld-aged formations with diamondiferous (diam., red) and non-diamondiferous (non-diam., yellow) kimberlites. (b) MT model at 125 km depth of the same region. (c) A - A' vertical section from the MT model. A - A' is indicated in (b). (d) Contour plot of the MT model. The 3D contour surface encloses regions with resistivities less than 100 Ωm. BC: Bushveld Complex, BCC: Bushveld Complex Conductor, Jw: Jwaneng Region, MFC: Molopo Farms Complex, MFCC: Molopo Farms Complex Conductor, MB: Magondi Belt, OkC: Okwa Complex, Prem: Premier Region, Sw: Swartruggens Region, RT: Rehoboth Terrain, KB: Kheis Belt, ZC: Zimbabwe Craton.

western pipes, the garnet xenocrysts from the pipes near the BC demonstrate higher whole-rock Al_2O_3, lower $Mg^{ol}\#$, a general increase in metasomatic classes and a lack of depleted material (Figure 5c,d,e).

The Palmietgat pipe is one of the very few kimberlite pipes emplaced near the centre of the BC (Figure 6i). Quite a high proportion of the garnets here (41%) do not fall into statistically significant CARP classifications associated with a consistent metasomatic signature. The high proportion of unclassified garnets at the Palmietgat pipe may indicate complex metasomatic overprinting, with multiple episodes of melts and fluids using the same conduits. A general increase in the proportion of unclassified samples near the BC can be seen in Figure 5f, suggesting the metasomatic signature in the area is highly complex.

The kimberlite cluster immediately west of or penetrating the western limb of the Bushveld Complex (Western Bushveld, Figure 6i) exhibits a thick layer of depleted lherzolites with phlogopite metasomatism between 130-160 km. Like other sections near the Bushveld Complex, many unclassified samples come from this middle section (130-170 km). These unclassified samples fall into wehrlite and low-Cr $CaO - Cr_2O_3$ classifications at the fertile layer and beneath the BDL, whereas they appear to be lherzolitic in the middle section. The Palmietfontein pipe (Figure S21c), like the Premier sections (Figure S22c), completely lacks samples from this middle section where the unclassified garnets are most populous.

Just south of the BC, the Premier kimberlite cluster (Figure 6j) is considerably older (928-1150 Ma) and yields higher equilibration temperatures ($40 mW/m^2$) compared to the Bushveld West cluster and the Palmietgat pipe (90-153 Ma, $38 mW/m^2$). The amount of secular cooling expected between 928 Ma and 153 Ma is around ($82 C^\circ$, Shu et al., 2014), a value similar to the difference in geotherms between the two clusters ($\sim 50-100 C^\circ$). Therefore, the area is not likely to have been impacted by a large thermal event between these times. This is consistent with the similarity of the geochemical 'tomography' sections showing a large portion of unclassified samples and depleted lherzolites with phlogopite metasomatism in the middle of the section. Like the Palmietfontein pipe of the Bushveld West cluster, the Premier and Franspoort pipes have entrained a relatively low number of garnets from this middle section (Figure S10c, S22c); it is probable that the strong metasomatism has destroyed most pre-existing garnet in the rocks at these levels.

The mantle beneath the Molopo Farms Complex (MFC), on the other hand, is sampled most closely by the Triassic-aged Jwaneng and Thankane kimberlite pipes (Figure 6d). The equilibration temperatures of the sampled xenocrysts are lower than in the BC (35 vs. 38 mW/m^2). The lower geotherm might indicate that the event that increased the geotherm beneath the Bushveld Complex, whether it be the main Bushveld event or not, did not affect the mantle near MFC at a similar scale. Geochemical stratification in these pipes is also more akin to the mantle beneath the Kimberley domain, where an increased population of depleted material is evident at mid-lithosphere depths. REE_N patterns display trends of metasomatic intensity at depths similar to those observed in Kimberley. A peak metasomatic intensity (lowest log-Nd_N Dy_N, highest Yb_N) is observed at 125 km (Figure S43). However, base-level rates of log-Nd_N Dy_N are much lower than the Kimberley (Figure 5g), suggesting metasomatic effects might be more extensive or that the area originally underwent less depletion.

5.3.2 Bushveld geoelectric structure and other geophysical studies

In our MT models, the Bushveld region shows marked lateral heterogeneity with some strongly conductive vertical sections extending towards the crust (e.g., BCC, Figure 9). The Thabazimbi-Murchison Lineament (TML) crosses three contrasting mantle electrical domains: a conductive lower lithospheric mantle and resistive upper litho-

spheric mantle in the vicinity of the Molopo Farms Complex, a resistive keel-like area beneath the Kanye Basin and a very conductive lithospheric mantle associated with the BC (Figure 9a). Broadly, such resistivity differences can either have thermal or compositional causes. S-wave seismic receiver function studies give no clear indication of a thinned mantle lithosphere beneath this region (Ravenna et al., 2018; Sodoudi et al., 2013). However, the Bushveld region is associated with lower S and P wave velocities (e.g., Ortiz et al., 2019; Youssof et al., 2013; Fouch et al., 2004) which suggests a chemical/metasomatic origin of the conductive anomalies rather than a thermal one (Griffin et al., 2009).

Seismic receiver function analyses indicate that the western-central area of the BC is marked by a relatively high crustal thickness ($\sim$ 49 km) with a more gradual Moho transition compared to sharper waveforms observed in the surrounding crust (Youssof et al., 2013; Delph & Porter, 2015). Kgaswane et al. (2012) also suggest structural complexity at crustal depths to account for observed receiver functions. The depressed Moho can be a sign of underplating by mafic intrusions (O'Reilly & Griffin, 2013). This anomalous zone overlies the Bushveld mantle conductor(BCC), extending from $>$ 200 km to near-surface where the MT transect crosses the TML. This region is a good candidate for a zone of mechanical weakness in the lithosphere where the Bushveld magmas could ascend and precipitate interconnected conductive minerals. The TML has been invoked many times before as the feeder location for the Bushveld magmatic units (e.g., Clarke et al., 2009). Such Moho complexity and localized increased Moho depths are not observed beneath the Molopo Farms Complex, which instead overlies gradual decreases in both Moho complexity and crustal thickness (Delph & Porter, 2015; Youssof et al., 2013).

The mantle beneath the Molopo Farms Complex has been modelled to be conductive at depths greater than $\sim$ 110 km but the resolution of this conductor is not robust and this feature is not as strong in the other inversion models (Moorkamp et al., 2021). At shallower depths, resistivities are comparable to the mantle beneath the Kanye Basin. If we assume similar parental magmas for the BC and MFC, the differences in resistivity of the mantle beneath them may suggest: (1) The magma emplacement that caused the MFC was not as focused as that which caused the BC, or the volume of magma intruding the lithosphere was smaller, (2) the MFC was not emplaced from deep feeder dykes but instead magmas flowed horizontally from the primary Bushveld magma source, most likely along the TML (Prendergast, 2012). Our models can not differentiate between these emplacement models but provide evidence for conductive metasomatic signatures beneath. However, if one expects similar mantle compositional sections from the BC and the MFC and a geotherm indicating lack of thermal impact beneath the MFC, the second option may seem more probable. A denser MT data collection around both areas may help to address this situation.

5.3.3 Compositional causes of conductivities

We have tested different compositional scenarios to fit the observed ranges of conductivity of the mantle beneath the Bushveld region. The thermal structure was constrained using the 38 mW/m^2 geotherm derived from garnet xenocryst data for the Cretaceous Group I kimberlites around the western lobe of the Bushveld Complex (Figure 6k) and the Jwaneng-Thankane pipes (35 mW/m^2). The Bushveld geotherm agrees well with other calculations derived from measured heat flow and crustal heat generation data (M. Jones, 2017). Similarly, thermobarometry data calculated with the method of Nimis & Taylor (2000) from Jwaneng samples fits a geotherm of 36.3 mW/m^2 (Figure S62, Preston & Sweeney, 2003). These results imply that with the maximum water contents allowed by the water solubility model (Padrón-Navarta & Hermann, 2017) and water-partitioning coefficients (Figure 10a, Demouchy et al., 2017), the water in NAMs in a lherzolitic mantle cannot explain the conductivities observed.

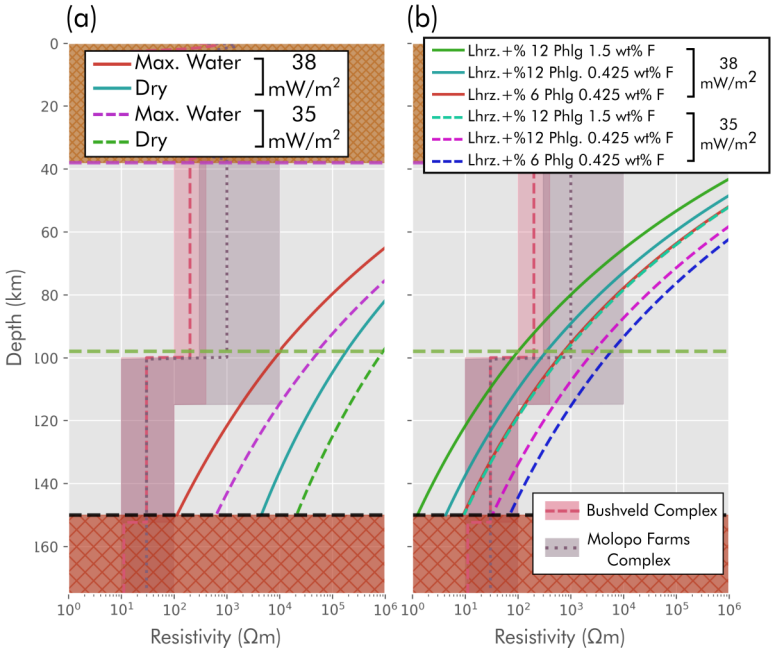

Figure 10. Comparisons between resistivities from the Bushveld and Molopo Farms complexes and theoretical calculations of electrical conductivity. (a) Bushveld Complex (red) and Molopo Farms (magenta) resistivities with resistivity depth curves calculated at hydration saturation determined using the olivine solubility model of Padrón-Navarta & Hermann (2017) and water-partitioning coefficients from Demouchy et al. (2017) and Novella et al. (2014) for pyroxenes and garnet, respectively. (b) Resistivity-depth curves calculated for a lherzolite composition with varying amounts of perfectly connected phlogopite. The electrical conductivity models used for the models are as follows: Olivine: Dai & Karato (2014), Orthopyroxene: Dai & Karato (2009a), Clinopyroxene: Liu et al. (2019), Garnet: Dai & Karato (2009b),Phlogopite: Y. Li et al. (2017).

Another possible explanation for such conductive mantle is the existence of well-connected fluorine-bearing phlogopite (Y. Li et al., 2017). Abundant phlogopite-style metasomatism is observed in almost all compositional sections near the Bushveld region (Figure 6). However, these signatures do not necessarily indicate the presence of perfectly connected phlogopite grains since they are the byproducts of reactions in which phlogopite replaces sparsely distributed garnets (Van Achterbergh et al., 2001). However, phlogopite could still precipitate on boundaries between NAM grains during percolation of metasomatic fluid or melt. Such a model with conductive phlogopites can also be envisioned as peridotites veined with MARID (Mica-Amphibole-Rutile-Ilmenite-Diopside) and PIC (Phlogopite-Ilmenite-Clinopyroxene) assemblages (Foley, 1992). This model of hydrous mineral emplacement is more likely to produce a mantle with highly interconnected phlogopite. We used the median F (fluorine) contents of glimmerite (MARID) xenoliths (~ 0.425 w.t.) as a realistic estimate and the maximum F content of all peridotite mantle xenoliths (~ 1.5 w.t.) as a bound on maximum conductivity that can be observed (Figure S61). For modal compositions, we derive a lherzolitic matrix with 12% and 6% of perfectly interconnected phlogopite. With these compositions, the conductivity of the mantle beneath Bushveld Complex can be explained below 100-120 km with 6% and 12 % phlogopite with 1.5 wt% and 0.425 wt% F, respectively. The same compositions would explain conductivities at relatively greater depths ($\sim 120 - 150$ km) in the colder mantle ($35\,mW/m^2$) beneath the Molopo Farms Complex.

It is impossible to model the conductor beneath the Bushveld Complex above 110 km (BCC) using experimental electrical conductivity data for the major rock-forming minerals existing in the mantle (olivine, pyroxenes, garnet, phlogopite and amphibole; Figure 10). Therefore, the conductivity requires minor accessory minerals such as graphite or sulphides, either as films on the edges of grains or as crystalline material precipitated from a metasomatic fluid (Pearson et al., 1994). However, the behaviour of these materials in a peridotitic matrix is not well understood, and some existing studies are in apparent conflict with each other (Wang et al., 2013; Zhang & Yoshino, 2017). Graphite, for instance, may establish an effective conductivity with higher than usual amounts of carbon in the mantle ($> 1.6\%$ vol., Wang et al., 2013). However, other authors suggest that graphite films are not stable with more realistic concentrations of carbon in the sample ($<< 0.8\%$ Zhang & Yoshino, 2017; Watson et al., 2010) and the previous results of Wang et al. (2013) may have only been the result of temporally limited crystallisation, which would not retain its interconnection given enough time (Zhang & Yoshino, 2017). Furthermore, the nature of carbon speciation in the mantle is not well understood, and the processes that bring xenoliths to the surface may result in compositionally biased xenolith samples (Stagno et al., 2019). For instance, some rare xenoliths from the Premier and Jagersfontein kimberlites are very rich in large veins of crystalline graphite (Pearson et al., 1994), suggesting that crystalline graphite might be underrepresented in xenoliths since they are likely to be destroyed by the carrier magma. On the other hand, the Palmietgat kimberlite is diamondiferous (Webb et al., 2011), which suggests the possible existence of graphite above the graphite-diamond transition.

Recent detailed studies on peridotite mixtures with magnetite (Dai et al., 2019) and chromite (W. Sun et al., 2021) showed that these types of minor constituents might have very different percolation thresholds before they dominate electrical conduction in an assemblage, probably reflecting their precipitation behaviour in the matrix. The percolation threshold represents the volume needed for a mineral to dominate the electrical conduction in an assemblage. While it is hard to reconcile any of the required volumetric abundances used in these experiments to reflect the actual state of the mantle (16% for chromite, 1.5% for magnetite), they illustrate the possibility that such phases could have a significant effect on metasomatised portions of the mantle.

Nevertheless, all Bushveld aged magmatism in the Kaapvaal Craton is strongly associated with a conductive signature in the MT models, which supports the idea that

the generation and emplacement of Bushveld magmas left a metasomatised signature in the lithospheric mantle (e.g., Zeh et al., 2015; Richardson & Shirey, 2008).

5.4 Namaqua-Natal Belt and Uintjiesberg

Southwest of the Kimberley area and over the proposed craton boundary, a different geoelectrical structure is apparent. Here, MT models indicate a lithosphere composed of a body (Eastern Namaqua-Belt Resistor, ENBR) that is highly resistive above 100-120 km and much less resistive below that depth (Figure 2a). Due to the thick Karoo sedimentary sequence, it is not entirely clear whether the southern limit of this resistive area is the border of the Kaapvaal Craton or not (Weckmann, 2012; Kobussen et al., 2008). However, the continuation of potential field lineaments alongside the Kheis Belt units suggests that the existing craton boundary coincides with our so-called suture zone (Corner & Durrheim, 2018). The significantly deeper Moho depths south of this boundary (Youssof et al., 2013; Delph & Porter, 2015) and the Proterozoic ages of the lower crustal granulite xenoliths from kimberlite clusters (Schmitz & Bowring, 2004) also suggests that the existing craton boundary runs through this location. We suggest that this resistor represents a Paleoproterozoic microcontinental block at the northernmost front of the Namaqua-Natal Belt where it collided with the Kaapvaal Craton.

Around the eastern Namaqua-Belt Resistor, the Uintjiesberg cluster consists of non- or weakly-diamondiferous Group I kimberlites (76-103 Ma, Figure 4a). Garnet xenocrysts indicate a mantle section with higher equilibration temperatures (40 mW/m^2) than the nearby Kimberley region (37 mW/m^2). The Group I thermal structure (Figure 4b), geoelectric architecture (Figure 2a) and calculated water contents (Figure 7) are consistent with a shallower base of the depleted lithosphere (135 km, Figure S40) and a higher proportion of melt-metasomatised classes, suggesting the region experienced extensive metasomatism during a thermal event (Kobussen et al., 2008). Differences in temperature and chemistry between Group I and Group II kimberlites in the region also suggest that extensive melt-infiltration and metasomatism occurred between these times, raising the base of the depleted lithosphere by $\sim$ 40 km (Kobussen et al., 2008).

From just above the base of the depleted lithosphere, a sudden drop in mean Ti/Zr ratios is evident and continues up to 110 km, suggesting phlogopite-related metasomatism at these depths. Considering that this layer (110-140 km) coincides with a layer of low resistivity in the MT models, it might be rich in interconnected phlogopites. However, electrical conductivity calculated with a perfectly connected phlogopite of 5-10 % with 0.425 wt% F is roughly an order of magnitude more conductive than modelled resistivities (Figure S6). This calculation indicates that electrical conductivities observed in the region are likely due to water in NAMs and not due to minor interconnected phlogopite. Fertile garnets in Uintjiesberg cluster also demonstrate the least sinuous patterns with strong HREE enrichment (Figure 5g,h). However, most of these garnets are between 100 and 110 km depth, where lower Ti/Zr values are not observed, suggesting that the metasomatic signature might not be as extensive at these depths.

5.5 Limpopo Belt

The Limpopo Belt is a continental block wedged between the Zimbabwe and Kaapvaal cratonic assemblages. Seismic tomography models demonstrate the existence of a thick cratonic lithosphere with fast velocities beneath the Limpopo Belt (Fouch et al., 2004; A. Li & Burke, 2006; Ortiz et al., 2019; Youssof et al., 2015). However, these models also show a seemingly fragmented structure, with relatively slower velocities in the eastern Limpopo Belt. These slower velocities may be attributed to metasomatism related to intense and pervasive Jurassic Karoo magmatism. Many authors have envisioned that the Karoo plume head was centred roughly on the eastern Limpopo Belt, based on the distribution of dyke swarms and volcanism radiating from the area (Figure 1, KTJ,

Jourdan et al., 2006). Whether or not the Karoo event was initiated by a mantle plume related to the Gondwana breakup, the eastern Limpopo Belt seems to be the centre of intense Jurassic volcanism.

Our MT models show that the Eastern Limpopo Belt comprises a highly conductive lower crust ($\leq 10\Omega m$) underlain by a highly conductive mantle. Sensitivity tests show the mantle between 50 to 100 km depth can be fit by a block with resistivities $\sim 60-100\Omega m$. Like the Bushveld Complex, the region also exhibits locally increased Moho depths with gradual velocity gradients (Youssof et al., 2013; Delph & Porter, 2015), which may suggest mafic underplating.

Garnet xenocrysts from kimberlites in the Venetia cluster, which was emplaced around the time of Gondwana assembly ($\sim 572-583$ Ma), indicate a considerable proportion of depleted harzburgites and lherzolites compared to the Kimberley area (Figure 6h). The high conductivity (Figure 6,2a) and lower seismic velocities modelled in the area do not reflect these garnet xenocryst compositions. The discrepancy between xenocrysts and geophysical models point to metasomatism of the lithospheric mantle that post-dated eruption of the Venetia kimberlites, likely to be effects of the $\sim 180Ma$ Karoo event, as previously suggested by Griffin et al. (2003).

5.6 Gibeon Fields

The Gibeon region stands out on the MT models with its resistive root and young, non-diamondiferous kimberlite cluster (Figure 6,11) around a relatively resistive region. The region is roughly situated within the Rehoboth Terrane along the boundary with the Namaqua-Natal Belt and is marked by a sudden drop in magnetic intensity (Corner & Durrheim, 2018). The kimberlites here are among the youngest in southern Africa ($60-72$ Ma) and are considered to be related to the same plume responsible for the emplacement of Group I kimberlites in Kimberley (Davies et al., 2001). Garnet xenocrysts shows a mantle section mostly made up of fertile lherzolites with relatively constant $Mg^{ol}\#$ (Figure 6a). Unlike what is observed in the Archean regions and the Uintjiesberg cluster, almost all of the fertile samples have high-Ti and low-Zr signatures likely to indicate low degrees of phlogopite metasomatism (Figure 5e). The geotherm derived from garnet xenocrysts can only be estimated from low temperature garnets while high temperature estimates seem to be scattered, similar to observations in other thermobarometric calculations (Bell et al., 2003) and likely to be an effect of melt-metasomatism beneath the depleted lithosphere. Two-pyroxene thermobarometry (Brey & Köhler, 1990) carried out by Bell et al. (2003) fits best to a conductive 41.5 mW/m^2 geotherm if the high temperature samples between 4-5 GPa are excluded. While these high temperature samples may indicate melt-related metasomatism, there is no indication of large scale melt infiltration in the geochemical tomography section and stable ($Mg^{ol}\# = 92$) values are observed.

Since the 3D MT model shows a highly resistive region with low estimated water contents, we propose that the mantle here might not be extensively metasomatised. The high resistivities suggest that there is no pervasive phlogopite metasomatism, while the abundant fertile lherzolites may indicate that the mantle never really experienced strong depletion. Due to a lack of data, we do not know whether this is a feature along the entire boundary between the Rehoboth Terrane and Namaqua-Natal Belt or if it is limited to the area around the Gibeon kimberlite field.

5.7 Distribution of kimberlites

Kimberlites are hydrous and carbonated volcanic rocks that originate from low-degree melting of the mantle below ~ 150 km (Giuliani et al., 2020). Because they ascend very rapidly (> 4 to 20 m/s, Sparks et al., 2006) and entrain xenoliths and xenocrysts from

surrounding wall-rock, they provide an invaluable window to the deeper mantle. The current most accepted mechanism for the faster ascent rates is crack-tip propagation via CO_2 exsolution, in which carbonated melts cleave the mantle by carbon degassing at the top of the percolation front while dissolving and assimilating orthopyroxene from the wall rock (Russell et al., 2012; Giuliani et al., 2020).

Clifford's rule (Clifford, 1966) suggests that diamondiferous kimberlites occur in terranes with Archean crust. Today we know that diamondiferous kimberlites frequently sample the cratonic mantle because diamonds are only stable below 130-150 km at colder cratonic geotherms (Day, 2012). Temporally, the genesis of kimberlites is linked to major tectonic events associated with global plate reorganisations such as the assembly and disruption of Gondwana (Jelsma et al., 2009). Spatially, kimberlites are mostly restricted to the edges of depleted cratonic keels comprised of chemically refertilised lithospheric mantle (Griffin et al., 2009; Faure et al., 2011). This specific spatiotemporal distribution of the kimberlites is correlated with fossil and active tectonic boundaries (Jelsma et al., 2004). These are commonly observed as lineaments in potential field geophysical studies (Corner & Durrheim, 2018), possibly indicating the tendency of kimberlites to use pre-existing zones of weakness in the lithosphere.

Through interpolated maximum resistivity maps of the lithospheric mantle, A. G. Jones et al. (2009) showed that kimberlites in southern Africa tend to concentrate near the edges of deep resistors that may correspond to depleted and dry cratonic keels. To compare the distribution of kimberlites and our magnetotelluric models, we made maps of mantle conductance ($\sum_{n=i}^{n} \sigma_i d_i$; i.e., integrated conductivity (σ) times thickness (d)) between 50-150 km (Figure 11a). Another map (Figure 11b) shows where the greatest depth to the 1000 Ωm value is observed. While containing similar information to the conductance map, this map emphasizes the spatial distribution of thick resistive roots. These maps demonstrate that kimberlites tend to be emplaced at the edges of the deepest and most resistive parts of the cratonic lithospheric mantle while also avoiding the most conductive parts.

One reason for the distribution of kimberlites around the deep resistors might be the inability of kimberlitic melts to penetrate thick and depleted cratonic roots. In such depleted regions, the kimberlite magmas may react with the refractory wall-rock materials to the extent that they cannot ascend to the surface (Giuliani et al., 2016). If these highly resistive keels have an orthopyroxene-poor ($< 15\%$) dunitic composition as suggested by some authors (e.g., Griffin et al., 2009), the rapid-ascent mechanism of crack-tip propagation via CO_2 degassing through assimilation of orthopyroxene from the wall rock might not operate efficiently (Russell et al., 2012). Generation of kimberlitic melt requires either the lithospheric mantle or the magma source beneath the lithosphere to be enriched in volatiles. This could be possible via metasomatism and carbonate freezing near the base of the lithosphere, including by Phanerozoic subduction processes (C. Sun & Dasgupta, 2020). A recent study suggests that the enriched signatures observed in kimberlite-hosted xenoliths globally reflect assimilated lithospheric mantle material (Giuliani et al., 2020). These factors also make penetration of kimberlites through deep resistors less likely, because higher water and carbon contents would be required to melt mantle peridotite in keels that extend to greater depths (Foley & Pintér, 2018) and thick Archean cratonic keels are unlikely to have been affected by subduction-related metasomatism. All of these things considered, it is more likely for kimberlites to episodically erupt at places that have previously been enriched in orthopyroxene, metasomatised and carbonated, and therefore have a moderate to low resistivity. Such events are more likely to concentrate around fossil continent/micro-continent collision zones with metasomatised compositions, as supported by correlations of kimberlite occurrences with magnetic and geological lineaments (Jelsma et al., 2004).

In the model, there are regions at the edges of the resistive roots ($> 1000\,\Omega m$) where the lithospheric mantle has lower resistivities (100-1000 Ωm) at depths greater than 100 km.

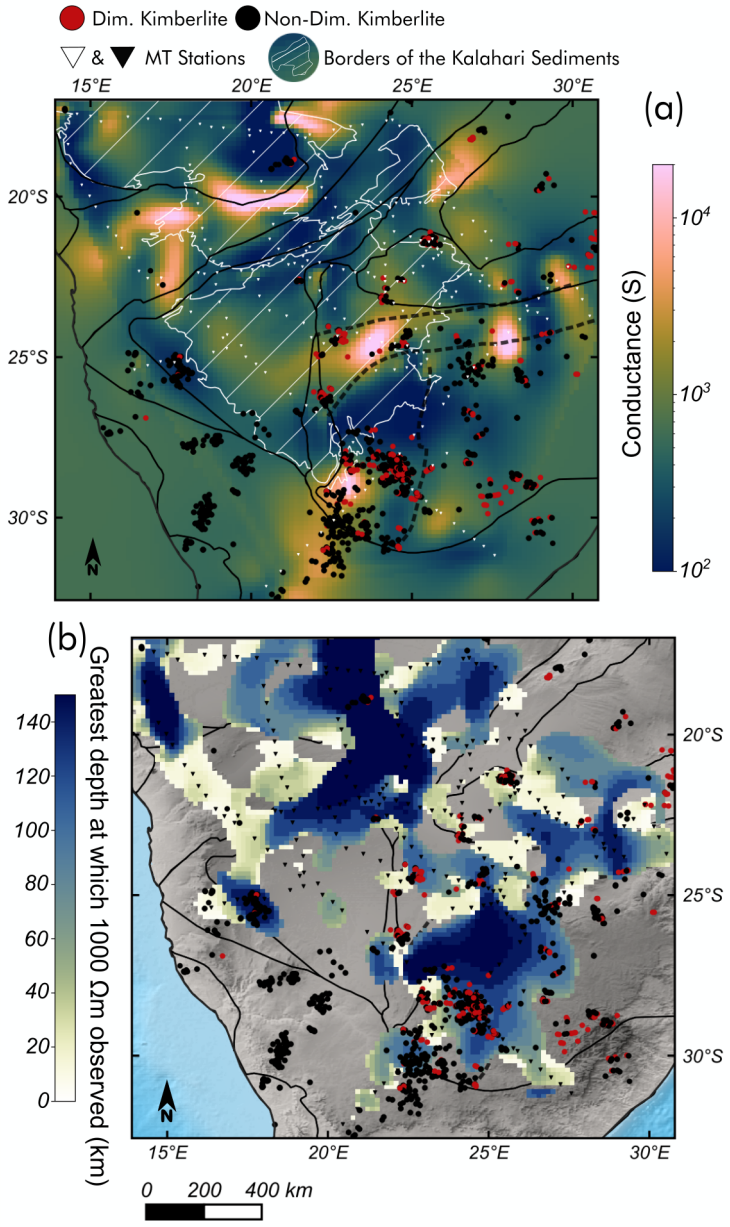

Figure 11. Distribution of kimberlites compared to (a) Lithospheric mantle conductance (from 50-200 km) and (b) The maximum depth at which a resistivity of 1000 Ωm is observed.

There are clear associations between these areas and kimberlite clusters (Figure 11) and almost all diamondiferous kimberlites occur within these relatively conductive zones. These conductive zones are indicated in Figure 11b as lighter blue areas usually appearing near darker blue, thick resistive zones. In contrast, non-diamondiferous kimberlites can be observed in these lower resistivity areas as well as in the more resistive portions of the cratons. These lower-resistivity regions are likely to have gone through broad-scale metasomatism, as also shown by their garnet xenocryst geochemical 'tomography' (Figure 6) and the compositions of whole-rock xenoliths, which include modal metasomatic minerals (e.g., Grégoire et al., 2003). Accordingly, a general recipe for diamond exploration with magnetotelluric data would be to search for regions located between the resistors of the cratonic nuclei and the conductors of metasomatised trans-lithospheric weakness zones.

On the other hand, it is not clear why kimberlite clusters avoid the prominent mantle conductors around the resistive cratonic nuclei. Similar behaviour has also been observed seismically, whereby kimberlites avoid regions of low shear wave velocity (Griffin et al., 2009). To examine this question further, detailed descriptions of these conductors have to be considered. One example of a prominent mantle conductor is the one at the southwest of the Kimberley area (SKC, Figure 2a,b). This conductor extends subvertically towards the surface at the edge of the craton where the Kheis Orogenic Belt and related fault systems are situated. This feature may be related to the collision between the proto-Namaqua-Natal Belt and the Kaapvaal Craton, and such conductors are often observed along fossil and active suture zones (e.g., Kelbert et al., 2019; Kirkby et al., 2020). Using the structural weakness corridor, Group I kimberlites may have further mineralised this pathway with rising metasomatic fluids. If kimberlites preferentially ascend along pre-existing zones of lithospheric weakness (e.g., Jelsma et al., 2004), this would be a perfect candidate. However, the area around this conductor contains only a few kimberlites, while most of the kimberlites in this region instead overlie relatively resistive mantle.

The absence of kimberlites associated with the Molopo Farms and Bushveld complex conductors may provide insight into the reasons kimberlites appear to avoid conductors more generally. Since both mantle conductors are associated with large mafic intrusions, one could argue that low-degree kimberlitic melts might have a rheological preference to move laterally along the contact with the Transvaal Basin when they meet the mafic material. This model could explain the near absence of kimberlites erupted over these conductors. Another possibility might be that a very depleted mantle exists near the base of the lithosphere (> 200 km) due to melt pooling in large volumes at this depth until it finally penetrates the lithospheric mantle. This model of Silver et al. (2006) is suggested to explain the very short duration ($< 1 m.y.$, Zeh et al., 2015) of emplacement of the Bushveld Complex. In such a scenario, kimberlites might not be able to penetrate this depleted layer or be generated within in due to low amounts of volatiles left in the layer after this massive melt extraction (Figure 12), similar to emplacement behaviour observed at resistive cratonic nuclei.

6 Concluding Remarks and Summary

3D MT models of southern Africa and geochemical information from garnet xenocrysts in Group I kimberlites are compared in the light of their tectonic and magmatic history. Both qualitative and quantitative interpretations were made for MT-derived composition analysis. Some of the most critical discussion points are:

- No general relationships can be made between the age of the terranes and conductivity distribution in the mantle since magmatic processes can either deplete or refertilise the lithospheric mantle.

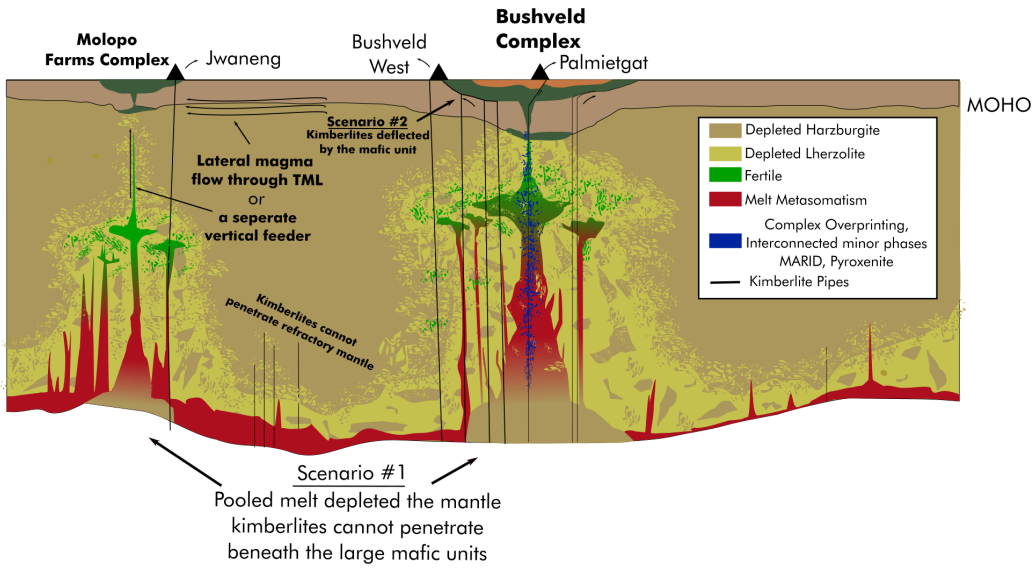

Figure 12. Conceptual sketch of our interpretation of mantle beneath the Bushveld Region. Scenarios 1 and 2 represents the possible reasons why kimberlites might avoid the center of the conductors. In Scenario 1, kimberlites avoid the conductors because they cannot penetrate or be generated within the depleted mantle formed by intense melt extraction during the Bushveld event. Scenario 2 posits the possibility that the kimberlites might be deflected by the mafic layer.

- Most of the Archean cratonic regions are imaged as relatively depleted regions with lower whole-rock Al_2O_3 values, higher mean $Mg^{ol}\#$, and a lower proportion of metasomatised CARP classes between 100-150 km. Some Archean areas around the Bushveld and Molopo Farms complexes appear to have a more fertile signature and metasomatised characteristics, matching well with electrically conductive mantle the large-scale magmatic event that occurred at 2.05 Ga.
- The area around the Bushveld Complex contains an increased proportion of unclassified garnets in the CARP classification scheme, suggesting either complex overprinting of multiple magmatic episodes. Conductivities below 100 km cannot be explained by water but can be explained by perfectly connected phlogopites. Conductivities above 100 km suggest that well-connected accessory minerals (e.g., sulfides, graphite or chromite) are likely to be present, precipitated extensively using the lithospheric weakness zone along the Thabazimbi-Murchison Lineament.
- The electrical conductivity of the cratonic mantle reflects the style of metasomatism, i.e., the composition of metasomatic fluids, how they were emplaced and the extent of the metasomatism, rather than reflecting simply the fertility of the mantle peridotite. This is best exemplified by the lithospheric mantle in the vicinity of Gibeon Fields, which is geochemically fertile yet highly resistive.
- Kimberlites in southern Africa are more likely to be observed around the edges of highly resistive mantle regions but also avoid the most conductive areas. They are most populous where the mantle below 100 km depth is relatively conductive. In resistive, depleted, orthopyroxene-poor and volatile-poor mantle, kimberlites are likely unable to penetrate through the mantle or cannot be generated.
- Conductive regions with no co-located kimberlites are usually associated with a mafic intrusion (e.g., Bushveld Complex, Molopo Farms Complex). We suggest this is due to: (1) A rheological preference of kimberlitic melts to intrude the contact with the sedimentary units when they meet the mafic layer; and/or (2) dur-

ing an event like Bushveld magmatism, in which significant volumes of magma are rapidly emplaced, volatiles near the lithosphere-asthenosphere boundary are also intensively extracted, created a zone where kimberlites either cannot penetrate or be generated.

Acronyms

BC Bushveld Complex
BDL Base of the Depleted Lithosphere
CARP Cluster Analysis by Regressive Partitioning
LIP Large Igneous Province
MT Magnetotelluric
MARID Mica-Amphibole-Rutile-Ilmenite-Diopside
MFC Molopo Farms Complex
NAMs Nominally Anhydrous Minerals
PGE Platinum-Group Elements
REE Rare-earth Elements
SAMTEX South African Magnetotelluric Experiment
SHF Surface Heat Flow
TML Thabazimbi-Murchison Lineament

Acknowledgments
This study was supported by Australian Research Council grant FT150100541. We thank the SAMTEX team for making the SAMTEX magnetotelluric dataset available at the IRIS SPUD repository (`https://doi.org/10.17611/DP/EMTF/SAMTEX`). We acknowledge the research funds for the TARDIS Project provided by the ARC Centre of Excellence for Core to Crust Fluid Systems (CCFS) and geochemical laboratory support through NCRIS AuScope and NSW Government Research Attraction and Acceleration Program grants. This is contribution XXX from the ARC Centre of Excellence for CCFS and YYY from the GEMOC Key Centre.

References

Afonso, J. C., Fernàndez, M., Ranalli, G., Griffin, W. L., & Connolly, J. A. (2008). Integrated geophysical-petrological modeling of the lithosphere and sublithospheric upper mantle: Methodology and applications. *Geochemistry, Geophysics, Geosystems*, *9*(5). doi: 10.1029/2007GC001834

Alard, O., Griffin, W. L., Lorand, J. P., Jackson, S. E., & O'Reilly, S. Y. (2000). Non-chondritic distribution of the highly siderophile elements in mantle sulphides. *Nature*, *407*(6806), 891–894.

Amante, C., & Eakins, B. (2009). Etopo1 1 arc-minute global relief model: procedures, data sources and analysis. noaa technical memorandum nesdis ngdc-24. *National Geophysical Data Center, NOAA*, *10*, V5C8276M.

Begg, G. C., Hronsky, J. A., Arndt, N. T., Griffin, W. L., O'Reilly, S. Y., & Hayward, N. (2010). Lithospheric, cratonic, and geodynamic setting of Ni-Cu-PGE sulfide deposits. *Economic Geology*, *105*(6), 1057–1070. doi: 10.2113/econgeo.105.6.1057

Bell, D. R., Ihinger, P. D., & Rossman, G. R. (1995, jun). Quantitative analysis of trace OH in garnet and pyroxenes. *American Mineralogist*, *80*(5-6), 465–474. doi: 10.2138/am-1995-5-607

Bell, D. R., Schmitz, M. D., & Janney, P. E. (2003). Mesozoic thermal evolution of

the southern African mantle lithosphere. *Lithos*, *71*(2-4), 273–287. doi: 10.1016/S0024-4937(03)00117-8

Beukes, N. J., de Kock, M. O., Vorster, C., Ravhura, L. G., Frei, D., Gumsley, A. P., & Harris, C. (2019). The age and country rock provenance of the Molopo farms complex: Implications for transvaal supergroup correlation in southern Africa. *South African Journal of Geology*, *122*(1), 39–56. doi: 10.25131/sajg.122.0003

Brey, G., & Köhler, T. (1990). Geothermobarometry in four-phase lherzolites ii. new thermobarometers, and practical assessment of existing thermobarometers. *Journal of Petrology*, *31*(6), 1353–1378. doi: 10.1016/0016-7037(90)90226-B

Cawthorn, R. G. (2015). The bushveld complex, south africa. In *Layered intrusions* (pp. 517–587). Springer.

Chisenga, C., Jianguo, Y., Fadel, I., van der Meijde, M., & Atekwana, E. A. (2020). Updated tectonic terrane boundaries of Botswana determined from gravity and aeromagnetic data. *Episodes*, *43*(4), 919–933. doi: 10.18814/EPIIUGS/2020/020054

Clarke, B., Uken, R., & Reinhardt, J. (2009). Structural and compositional constraints on the emplacement of the Bushveld Complex, South Africa. *Lithos*, *111*(1-2), 21–36. doi: 10.1016/j.lithos.2008.11.006

Clifford, T. N. (1966). Tectono-metallogenic units and metallogenic provinces of Africa. *Earth and Planetary Science Letters*, *1*(6), 421–434. doi: 10.1016/0012-821X(66)90039-2

Cole, J., Webb, S. J., & Finn, C. A. (2014). Gravity models of the Bushveld Complex - Have we come full circle? *Journal of African Earth Sciences*, *92*, 97–118. doi: 10.1016/j.jafrearsci.2014.01.012

Corner, B., & Durrheim, R. J. (2018). An integrated geophysical and geological interpretation of the southern african lithosphere. In *Geology of southwest gondwana* (pp. 19–61). Springer.

Dai, L., Hu, H., Sun, W., Li, H., Liu, C., & Wang, M. (2019). Influence of high conductive magnetite impurity on the electrical conductivity of dry olivine aggregates at high temperature and high pressure. *Minerals*, *9*(1). doi: 10.3390/min9010044

Dai, L., & Karato, S.-i. (2009a). Electrical conductivity of orthopyroxene: Implications for the water content of the asthenosphere. *Proceedings of the Japan Academy, Series B*, *85*(10), 466–475. doi: 10.2183/pjab.85.466

Dai, L., & Karato, S.-i. (2009b). Electrical conductivity of pyrope-rich garnet at high temperature and high pressure. *Physics of the Earth and Planetary Interiors*, *176*(1-2), 83–88. doi: 10.1016/j.pepi.2009.04.002

Dai, L., & Karato, S.-i. (2014). High and highly anisotropic electrical conductivity of the asthenosphere due to hydrogen diffusion in olivine. *Earth and Planetary Science Letters*, *408*, 79–86. doi: 10.1016/j.epsl.2014.10.003

Davies, G. R., Spriggs, A. J., & Nixon, P. H. (2001). A non-cognate origin for the Gibeon kimberlite megacryst suite, Namibia: Implications for the origin of Namibian kimberlites. *Journal of Petrology*, *42*(1), 159–172. doi: 10.1093/petrology/42.1.159

Davis, G. L. (1977). The ages and uranium contents of zircons from kimberlites and associated rocks. In *International kimberlite conference: Extended abstracts* (Vol. 2, pp. 67–69).

Dawson, J. B., & Stephens, W. (1975). Statistical classification of garnets from kimberlite and associated xenoliths. *The Journal of Geology*, *83*(5), 589–607.

Day, H. W. (2012). A revised diamond-graphite transition curve. *American Mineralogist*, *97*(1), 52–62. doi: 10.2138/am.2011.3763

De Kock, M. O., Ernst, R., Söderlund, U., Jourdan, F., Hofmann, A., Le Gall, B., ... Fuchs, R. (2014). Dykes of the 1.11Ga Umkondo LIP, Southern Africa: Clues to a complex plumbing system. *Precambrian Research*, *249*, 129–143. doi: 10.1016/j.precamres.2014.05.006

De Wit, M. J., De Ronde, C. E., Tredoux, M., Roering, C., Hart, R. J., Armstrong, R. A., ... Hart, R. A. (1992, jun). Formation of an Archaean continent. *Nature*, *357*(6379), 553–562. doi: 10.1038/357553a0

De Beer, J. H. (2016). *The history of geophysics in southern africa.* African Sun Media.

Delph, J. R., & Porter, R. C. (2015). Crustal structure beneath southern Africa: Insight into how tectonic events affect the Mohorovičić discontinuity. *Geophysical Journal International*, *200*(1), 254–264. doi: 10.1093/gji/ggu376

Demouchy, S., & Bolfan-Casanova, N. (2016). Distribution and transport of hydrogen in the lithospheric mantle: A review. *Lithos*, *240-243*, 402–425. doi: 10.1016/j.lithos.2015.11.012

Demouchy, S., Shcheka, S., Denis, C. M., & Thoraval, C. (2017). Subsolidus hydrogen partitioning between nominally anhydrous minerals in garnet-bearing peridotite. *American Mineralogist*, *102*(9), 1822–1831. doi: 10.2138/am-2017-6089

Evans, R. L., Jones, A. G., Garcia, X., Muller, M., Hamilton, M., Evans, S., ... Hutchins, D. (2011). Electrical lithosphere beneath the Kaapvaal craton, southern Africa. *Journal of Geophysical Research: Solid Earth*, *116*(4), 1–16. doi: 10.1029/2010JB007883

Faure, S., Godey, S., Fallara, F., & Trépanier, S. (2011). Seismic architecture of the archean north american mantle and its relationship to diamondiferous kimberlite fields. *Economic Geology*, *106*(2), 223–240. doi: 10.2113/econgeo.106.2.223

Férot, A., & Bolfan-Casanova, N. (2012). Water storage capacity in olivine and pyroxene to 14GPa: Implications for the water content of the Earth's upper mantle and nature of seismic discontinuities. *Earth and Planetary Science Letters*, *349-350*, 218–230. doi: 10.1016/j.epsl.2012.06.022

Foley, S. F. (1992). Vein-plus-wall-rock melting mechanisms in the lithosphere and the origin of potassic alkaline magmas. *Lithos*, *28*(3-6), 435–453. doi: 10.1016/0024-4937(92)90018-T

Foley, S. F., & Pintér, Z. (2018). *Primary Melt Compositions in the Earth's Mantle.* doi: 10.1016/B978-0-12-811301-1.00001-0

Fouch, M. J., James, D. E., VanDecar, J. C., & van der Lee, S. (2004). Mantle seismic structure beneath the Kaapvaal and Zimbabwe Cratons. *South African Journal of Geology*, *107*(1-2), 33–44. doi: 10.2113/107.1-2.33

Gardés, E., Gaillard, F., & Tarits, P. (2014, dec). Toward a unified hydrous olivine electrical conductivity law. *Geochemistry, Geophysics, Geosystems*, *15*(12), 4984–5000. Retrieved from `http://doi.wiley.com/10.1002/2014GC005496` doi: 10.1002/2014GC005496

Gaul, O. F., Griffin, W. L., O'Reilly, S. Y., & Pearson, N. J. (2000). Mapping olivine composition in the lithospheric mantle. *Earth and Planetary Science Letters*, *182*(3-4), 223–235. doi: 10.1016/S0012-821X(00)00243-0

Giuliani, A., Graham Pearson, D., Soltys, A., Dalton, H., Phillips, D., Foley, S. F., ... Mitchell, R. H. (2020). Kimberlite genesis from a common carbonate-rich primary melt modified by lithospheric mantle assimilation. *Science Advances*, *6*(17), 1–10. doi: 10.1126/sciadv.aaz0424

Giuliani, A., Phillips, D., Kamenetsky, V. S., & Goemann, K. (2016). Constraints on kimberlite ascent mechanisms revealed by phlogopite compositions in kimberlites and mantle xenoliths. *Lithos*, *240-243*(2016), 189–201. doi: 10.1016/j.lithos.2015.11.013

Giuliani, A., Phillips, D., Woodhead, J. D., Kamenetsky, V. S., Fiorentini, M. L., Maas, R., ... Armstrong, R. A. (2015). Did diamond-bearing orangeites originate from MARID-veined peridotites in the lithospheric mantle? *Nature Communications*, *6*. doi: 10.1038/ncomms7837

Glover, P. W. J. (2010). A generalized Archie's law for n phases. *Geophysics*, *75*(6), E247–E265. doi: 10.1190/1.3509781

Good, N., & De Wit, M. J. (1997). The Thabazimbi-Murchison lineament of the Kaapvaal Craton, South Africa: 2700 Ma of episodic deformation. *Journal of the Geological Society*, *154*(1), 93–97. doi: 10.1144/gsjgs.154.1.0093

Goscombe, B., Foster, D. A., Gray, D., Wade, B., Marsellos, A., & Titus, J. (2017). Deformation correlations, stress field switches and evolution of an orogenic intersection: The Pan-African Kaoko-Damara orogenic junction, Namibia. *Geoscience Frontiers*, *8*(6), 1187–1232. doi: 10.1016/j.gsf.2017.05.001

Grégoire, M., Bell, D. R., & Le Roex, A. P. (2003). Garnet lherzolites from the Kaapvaal Craton (South Africa): Trace element evidence for a metasomatic history. *Journal of Petrology*, *44*(4), 629–657. doi: 10.1093/petrology/44.4.629

Griffin, W. L., Begg, G. C., & O'Reilly, S. Y. (2013). Continental-root control on the genesis of magmatic ore deposits. *Nature Geoscience*, *6*(11), 905–910. doi: 10.1038/ngeo1954

Griffin, W. L., Fisher, N. I., Friedman, J. H., O'Reilly, S. Y., & Ryan, C. G. (2002). Cr-pyrope garnets in the lithospheric mantle 2. Compositional populations and their distribution in time and space. *Geochemistry, Geophysics, Geosystems*, *3*(12), 1–35. doi: 10.1029/2002gc000298

Griffin, W. L., O'Reilly, S. Y., Afonso, J. C., & Begg, G. C. (2009). The composition and evolution of lithospheric mantle: A re-evaluation and its tectonic implications. *Journal of Petrology*, *50*(7), 1185–1204. doi: 10.1093/petrology/egn033

Griffin, W. L., O'Reilly, S. Y., Natapov, L. M., & Ryan, C. G. (2003). The evolution of lithospheric mantle beneath the Kalahari Craton and its margins. *Lithos*, *71*(2-4), 215–241. doi: 10.1016/j.lithos.2003.07.006

Griffin, W. L., Shee, S. R., Ryan, C. G., Win, T. T., & Wyatt, B. A. (1999). Harzburgite to lherzolite and back again: metasomatic processes in ultramafic xenoliths from the Wesselton kimberlite, Kimberley, South Africa. *Contrib Mineral Petrol*, *134*, 232–250.

Grütter, H. S., Gurney, J. J., Menzies, A. H., & Winter, F. (2004). An updated classification scheme for mantle-derived garnet, for use by diamond explorers. *Lithos*, *77*(1-4), 841–857.

Gumsley, A., Stamsnijder, J., Larsson, E., Söderlund, U., Naeraa, T., De Kock, M., ... Ernst, R. (2020). Neoarchean large igneous provinces on the Kaapvaal Craton in southern Africa re-define the formation of the Ventersdorp Supergroup and its temporal equivalents. *Bulletin of the Geological Society of America*, *132*(9-10), 1829–1844. doi: 10.1130/B35237.1

Hanson, R. E. (2003). Proterozoic geochronology and tectonic evolution of southern Africa. *Geological Society Special Publication*, *206*, 427–463.

Hanson, R. E., Harmer, R. E., Blenkinsop, T. G., Bullen, D. S., Dalziel, I. W., Gose, W. A., ... Ward, S. E. (2006). Mesoproterozoic intraplate magmatism in the Kalahari Craton: A review. *Journal of African Earth Sciences*, *46*(1-2), 141–167. doi: 10.1016/j.jafrearsci.2006.01.016

Hasterok, D., & Chapman, D. S. (2011). Heat production and geotherms for the continental lithosphere. *Earth and Planetary Science Letters*, *307*(1-2), 59–70. doi: 10.1016/j.epsl.2011.04.034

Humbert, F., de Kock, M., Lenhardt, N., & Altermann, W. (2019). Neoarchaean to early palaeoproterozoic within-plate volcanism of the kaapvaal craton: Comparing the ventersdorp supergroup and the ongeluk and hekpoort formations (transvaal supergroup). In *The archaean geology of the kaapvaal craton, southern africa* (pp. 277–302). Springer.

Jacobs, J., Pisarevsky, S., Thomas, R. J., & Becker, T. (2008). The Kalahari Craton during the assembly and dispersal of Rodinia. *Precambrian Research*, *160*(1-2), 142–158. doi: 10.1016/j.precamres.2007.04.022

Jelsma, H. A., Barnett, W., Richards, S., & Lister, G. (2009). Tectonic setting of kimberlites. *Lithos*, *112*, 155–165. doi: 10.1016/j.lithos.2009.06.030

Jelsma, H. A., de Wit, M. J., Thiart, C., Dirks, P. H., Viola, G., Basson, I. J., & Anckar, E. (2004). Preferential distribution along transcontinental corridors of kimberlites and related rocks of Southern Africa. *South African Journal of Geology*, *107*(1-2), 301–324. doi: 10.2113/107.1-2.301

Jones, A. G., Evans, R. L., Muller, M. R., Hamilton, M. P., Miensopust, M. P., Garcia, X., ... Wasborg, J. (2009). Area selection for diamonds using magnetotellurics: Examples from southern Africa. *Lithos*, *112*, 83–92. doi: 10.1016/j.lithos.2009.06.011

Jones, M. (2017). Heat flow in the Bushveld Complex, South Africa: implications for upper mantle structure. *South African Journal of Geology*, *120*(3), 351–370. doi: 10.25131/gssajg.120.3.351

Jourdan, F., Féraud, G., Bertrand, H., Watkeys, M. K., Kampunzu, A. B., & Le Gall, B. (2006). Basement control on dyke distribution in Large Igneous Provinces: Case study of the Karoo triple junction. *Earth and Planetary Science Letters*, *241*(1-2), 307–322. doi: 10.1016/j.epsl.2005.10.003

Kaavera, J., Rajesh, H. M., Tsunogae, T., & Belyanin, G. A. (2018). Marginal facies and compositional equivalents of Bushveld parental sills from the Molopo Farms Complex layered intrusion, Botswana: Petrogenetic and mineralization implications. *Ore Geology Reviews*, *92*(November 2017), 506–528. doi: 10.1016/j.oregeorev.2017.12.001

Karato, S.-i., & Wang, D. (2012). Electrical conductivity of minerals and rocks. *Physics and Chemistry of the Deep Earth*, 145–236.

Kelbert, A., Bedrosian, P. A., & Murphy, B. S. (2019). The first 3D conductivity model of the contiguous United States: Reflections on geologic structure and application to induction hazards. *Geomagnetically Induced Currents from the Sun to the Power Grid*, 127–151. doi: 10.1002/9781119434412.ch8

Kelbert, A., Meqbel, N., Egbert, G. D., & Tandon, K. (2014). ModEM: A modular system for inversion of electromagnetic geophysical data. *Computers and Geosciences*, *66*, 40–53. doi: 10.1016/j.cageo.2014.01.010

Kgaswane, E. M., Nyblade, A. A., Durrheim, R. J., Julià, J., Dirks, P. H. G. M., & Webb, S. J. (2012). Shear wave velocity structure of the Bushveld Complex, South Africa. *Tectonophysics*, *554-557*, 83–104. doi: 10.1016/j.tecto.2012.06.003

Khoza, D., Jones, A. G., Muller, M. R., Evans, R. L., Miensopust, M. P., & Webb, S. J. (2013a). Lithospheric structure of an Archean craton and adjacent mobile belt revealed from 2-D and 3-D inversion of magnetotelluric data: Example from southern Congo craton in northern Namibia. *Journal of Geophysical Research: Solid Earth*, *118*(8), 4378–4397. doi: 10.1002/jgrb.50258

Khoza, D., Jones, A. G., Muller, M. R., Evans, R. L., Webb, S. J., & Miensopust, M. (2013b). Tectonic model of the Limpopo belt: Constraints from magnetotelluric data. *Precambrian Research*, *226*, 143–156. doi: 10.1016/j.precamres.2012.11.016

Kirkby, A. L., Musgrave, R. J., Czarnota, K., Doublier, M. P., Duan, J., Cayley, R. A., & Kyi, D. (2020). Lithospheric architecture of a Phanerozoic orogen from magnetotellurics: AusLAMP in the Tasmanides, southeast Australia. *Tectonophysics*, *793*(November 2019), 228560. doi: 10.1016/j.tecto.2020.228560

Kobussen, A. F., Griffin, W. L., & O'Reilly, S. Y. (2009). Cretaceous thermochemical modification of the Kaapvaal cratonic lithosphere, South Africa. *Lithos*, *112*, 886–895. doi: 10.1016/j.lithos.2009.06.031

Kobussen, A. F., Griffin, W. L., O'Reilly, S. Y., & Shee, S. R. (2008). Ghosts of lithospheres past: Imaging an evolving lithospheric mantle in southern Africa. *Geology*, *36*(7), 515–518. doi: 10.1130/G24868A.1

Kruger, F. J. (2005). Filling the Bushveld Complex magma chamber: Lateral expansion, roof and floor interaction, magmatic unconformities, and the formation of giant chromitite, PGE and Ti-V-magnetitite deposits. *Mineralium Deposita*,

40(5), 451–472. doi: 10.1007/s00126-005-0016-8

Laurent, O., Zeh, A., Brandl, G., Vezinet, A., & Wilson, A. (2019). Granitoids and greenstone belts of the pietersburg block—witnesses of an archaean accretionary orogen along the northern edge of the kaapvaal craton. In *The archaean geology of the kaapvaal craton, southern africa* (pp. 83–107). Springer.

Li, A., & Burke, K. (2006). Upper mantle structure of southern Africa from Rayleigh wave tomography. *Journal of Geophysical Research: Solid Earth*, *111*(10), 1–16. doi: 10.1029/2006JB004321

Li, Y., Jiang, H., & Yang, X. (2017). Fluorine follows water: Effect on electrical conductivity of silicate minerals by experimental constraints from phlogopite. *Geochimica et Cosmochimica Acta*, *217*, 16–27. doi: 10.1016/j.gca.2017.08.020

Liu, H., Zhu, Q., & Yang, X. (2019). Electrical conductivity of OH-bearing omphacite and garnet in eclogite: the quantitative dependence on water content. *Contributions to Mineralogy and Petrology*, *174*(7), 1–15. doi: 10.1007/s00410-019-1593-3

Maier, W. D., Peltonen, P., Grantham, G., & Mänttäri, I. (2003). A new 1.9 Ga age for the Trompsburg intrusion, South Africa. *Earth and Planetary Science Letters*, *212*(3-4), 351–360. doi: 10.1016/S0012-821X(03)00281-4

Master, S., Bekker, A., & Hofmann, A. (2010). A review of the stratigraphy and geological setting of the Palaeoproterozoic Magondi Supergroup, Zimbabwe - Type locality for the Lomagundi carbon isotope excursion. *Precambrian Research*, *182*(4), 254–273. doi: 10.1016/j.precamres.2010.08.013

McCourt, S., Armstrong, R. A., Jelsma, H., & Mapeo, R. B. (2013). New U-Pb SHRIMP ages from the Lubango region, SW Angola: Insights into the Palaeoproterozoic evolution of the Angolan Shield, southern Congo Craton, Africa. *Journal of the Geological Society*, *170*(2), 353–363. doi: 10.1144/jgs2012-059

Miensopust, M. P., Jones, A. G., Muller, M. R., Garcia, X., & Evans, R. L. (2011). Lithospheric structures and Precambrian terrane boundaries in northeastern Botswana revealed through magnetotelluric profiling as part of the Southern African Magnetotelluric Experiment. *Journal of Geophysical Research: Solid Earth*, *116*(2), 1–21. doi: 10.1029/2010JB007740

Modie, B. N. (2000). Geology and mineralisation in the meso-to neoproterozoic ghanzi-chobe belt of northwest botswana. *Journal of African Earth Sciences*, *30*(3), 467–474.

Moorkamp, M., Fishwick, S., Walker, R. J., & Jones, A. G. (2019). Geophysical evidence for crustal and mantle weak zones controlling intra-plate seismicity – the 2017 Botswana earthquake sequence. *Earth and Planetary Science Letters*, *506*, 175–183. doi: 10.1016/j.epsl.2018.10.048

Moorkamp, M., Heincke, B., Jegen, M., Roberts, A. W., & Hobbs, R. W. (2011). A framework for 3-d joint inversion of mt, gravity and seismic refraction data. *Geophysical Journal International*, *184*(1), 477–493.

Moorkamp, M., Özaydın, S., Selway, K., Griffin, W., & Jones, A. G. (2021). A large scale conductivity model for southern africa. *Journal of Geophysical Research: Solid Earth*, *submitted*.

Muller, M. R., Jones, A. G., Evans, R. L., Grütter, H. S., Hatton, C., Garcia, X., ... Wasborg, J. (2009). Lithospheric structure, evolution and diamond prospectivity of the Rehoboth Terrane and western Kaapvaal Craton, southern Africa: Constraints from broadband magnetotellurics. *Lithos*, *112*, 93–105. doi: 10.1016/j.lithos.2009.06.023

Nimis, P., & Taylor, W. R. (2000). Single clinopyroxene thermobarometry for garnet peridotites. part i. calibration and testing of a cr-in-cpx barometer and an enstatite-in-cpx thermometer. *Contributions to Mineralogy and Petrology*, *139*(5), 541–554.

Novella, D., Frost, D. J., Hauri, E. H., Bureau, H., Raepsaet, C., & Roberge, M.

(2014). The distribution of H2O between silicate melt and nominally anhydrous peridotite and the onset of hydrous melting in the deep upper mantle. *Earth and Planetary Science Letters*, *400*, 1–13. doi: 10.1016/j.epsl.2014.05.006

O'Reilly, S. Y., & Griffin, W. (2006). Imaging global chemical and thermal heterogeneity in the subcontinental lithospheric mantle with garnets and xenoliths: Geophysical implications. *Tectonophysics*, *416*(1-4), 289–309.

O'Reilly, S. Y., & Griffin, W. (2013). Moho vs crust–mantle boundary: evolution of an idea. *Tectonophysics*, *609*, 535–546.

Oriolo, S., & Becker, T. (2018). The kalahari craton, southern africa: from archean crustal evolution to gondwana amalgamation. In *Geology of southwest gondwana* (pp. 133–159). Springer.

Ortiz, K., Nyblade, A., van der Meijde, M., Paulssen, H., Kwadiba, M., Ntibinyane, O., ... Homman, K. (2019). Upper Mantle P and S Wave Velocity Structure of the Kalahari Craton and Surrounding Proterozoic Terranes, Southern Africa. *Geophysical Research Letters*, *46*(16), 9509–9518. doi: 10.1029/2019GL084053

Özaydın, S., & Selway, K. (2020). MATE: An analysis tool for the interpretation of magnetotelluric models of the mantle. *Geochemistry, Geophysics, Geosystems*, 1–26. doi: 10.1029/2020gc009126

Özaydın, S., Selway, K., & Griffin, W. L. (2021). Are xenoliths from southwestern Kaapvaal Craton representative of the broader mantle? Constraints from magnetotelluric modeling. *Geophysical Research Letters*, *48*, 1-11. doi: 10.1029/2021GL092570

Padrón-Navarta, J. A., & Hermann, J. (2017). A Subsolidus Olivine Water Solubility Equation for the Earth's Upper Mantle. *Journal of Geophysical Research: Solid Earth*, *122*(12), 9862–9880. doi: 10.1002/2017JB014510

Palme, H., & O'Neill, H. (2013). *Cosmochemical Estimates of Mantle Composition* (2nd ed., Vol. 3). Elsevier Ltd. doi: 10.1016/B978-0-08-095975-7.00201-1

Pearson, D. G., Boyd, F. R., Haggerty, S. E., Pasteris, J. D., Field, S. W., Nixon, P. H., & Pokhilenko, N. P. (1994). The characterisation and origin of graphite in cratonic lithospheric mantle: a petrological carbon isotope and Raman spectroscopic study. *Contributions to Mineralogy and Petrology*, *115*(4), 449–466. doi: 10.1007/BF00320978

Pearson, D. G., Irvine, G. J., Ionov, D. A., Boyd, F. R., & Dreibus, G. E. (2004). Re-Os isotope systematics and platinum group element fractionation during mantle melt extraction: A study of massif and xenolith peridotite suites. *Chemical Geology*, *208*(1-4), 29–59. doi: 10.1016/j.chemgeo.2004.04.005

Poujol, M., Robb, L. J., Anhaeusser, C. R., & Gericke, B. (2003). A review of the geochronological constraints on the evolution of the Kaapvaal Craton, South Africa. *Precambrian Research*, *127*(1-3), 181–213. doi: 10.1016/S0301-9268(03)00187-6

Prendergast, M. D. (2012). The molopo farms complex, southern botswana - A reconsideration of structure, evolution, and the bushveld connection. *South African Journal of Geology*, *115*(1), 77–90. doi: 10.2113/gssajg.115.1.77

Preston, R., & Sweeney, R. (2003). A comparison of clinopyroxene thermobarometric techniques: applied to jwaneng, orapa and markt kimberlites. In *International kimberlite conference: Extended abstracts* (Vol. 8).

Rajesh, H. M., Chisonga, B. C., Shindo, K., Beukes, N. J., & Armstrong, R. A. (2013). Petrographic, geochemical and SHRIMP U-Pb titanite age characterization of the Thabazimbi mafic sills: Extended time frame and a unifying petrogenetic model for the Bushveld Large Igneous Province. *Precambrian Research*, *230*, 79–102. doi: 10.1016/j.precamres.2013.02.002

Ravenna, M., Lebedev, S., Fullea, J., & Adam, J. M. (2018). Shear-Wave Velocity Structure of Southern Africa's Lithosphere: Variations in the Thickness and Composition of Cratons and Their Effect on Topography. *Geochemistry, Geophysics,*

Geosystems, *19*(5), 1499–1518. doi: 10.1029/2017GC007399

Rezaie, M., Moradzadeh, A., Kalate, A. N., Aghajani, H., Kahoo, A. R., & Moazam, S. (2017). 3D modelling of Trompsburg Complex (in South Africa) using 3D focusing inversion of gravity data. *Journal of African Earth Sciences*, *130*, 1–7. doi: 10.1016/j.jafrearsci.2017.03.002

Richardson, S. H., & Shirey, S. B. (2008). Continental mantle signature of Bushveld magmas and coeval diamonds. *Nature*, *453*(7197), 910–913. doi: 10.1038/nature07073

Russell, J. K., Porritt, L. A., Lavallée, Y., & Dingwell, D. B. (2012). Kimberlite ascent by assimilation-fuelled buoyancy. *Nature*, *481*(7381), 352–356.

Ryan, C. G., Griffin, W. L., & Pearson, N. J. (1996). Garnet geotherms: Pressure-temperature data from Cr-pyrope garnet xenocrysts in volcanic rocks. *Journal of Geophysical Research: Solid Earth*, *101*(B3), 5611–5625. doi: 10.1029/95JB03207

Schmitz, M. D., & Bowring, S. A. (2004). Lower crustal granulite formation during Mesoproterozoic Namaqua-Natal collisional orogenesis, southern Africa. *South African Journal of Geology*, *107*(1-2), 261–284. doi: 10.2113/107.1-2.261

Scoates, J. S., Wall, C. J., Friedman, R. M., Weis, D., Mathez, E. A., & VanTongeren, J. A. (2021). Dating the Bushveld Complex: Timing of Crystallization, Duration of Magmatism, and Cooling of the World's Largest Layered Intrusion and Related Rocks. *Journal of Petrology*(604). doi: 10.1093/petrology/egaa107

Selway, K. (2015). Negligible effect of hydrogen content on plate strength in East Africa. *Nature Geoscience*, *8*(7), 543–546. doi: 10.1038/ngeo2453

Selway, K., Hand, M., Payne, J. L., Heinson, G. S., & Reid, a. (2011). Magnetotelluric constraints on the tectonic setting of Grenville-aged orogenesis in central Australia. *Journal of the Geological Society*, *168*, 251–264. doi: 10.1144/0016-76492010-034

Selway, K., O'Donnell, J. P., & Özaydin, S. (2019, jul). Upper Mantle Melt Distribution From Petrologically Constrained Magnetotellurics. *Geochemistry, Geophysics, Geosystems*, 2019GC008227. doi: 10.1029/2019GC008227

Shu, Q., Brey, G. P., Gerdes, A., & Hoefer, H. E. (2014). Mantle eclogites and garnet pyroxenites - the meaning of two-point isochrons, Sm-Nd and Lu-Hf closure temperatures and the cooling of the subcratonic mantle. *Earth and Planetary Science Letters*, *389*, 143–154. doi: 10.1016/j.epsl.2013.12.028

Silver, P. G., Behn, M. D., Kelley, K., Schmitz, M., & Savage, B. (2006). Understanding cratonic flood basalts. *Earth and Planetary Science Letters*, *245*(1-2), 190–201. doi: 10.1016/j.epsl.2006.01.050

Sodoudi, F., Yuan, X., Kind, R., Lebedev, S., Adam, J. M., Kästle, E., & Tilmann, F. (2013). Seismic evidence for stratification in composition and anisotropic fabric within the thick lithosphere of Kalahari Craton. *Geochemistry, Geophysics, Geosystems*, *14*(12), 5393–5412. doi: 10.1002/2013GC004955

Sparks, R., Baker, L., Brown, R., Field, M., Schumacher, J., Stripp, G., & Walters, A. (2006). Dynamical constraints on kimberlite volcanism. *Journal of Volcanology and Geothermal Research*, *155*(1-2), 18–48.

Stagno, V., Cerantola, V., Aulbach, S., Lobanov, S., McCammon, C. A., & Merlini, M. (2019). Carbon-bearing phases throughout earth's interior. In *Deep carbon: Past to present* (pp. 66–88). Cambridge University Press.

Sun, C., & Dasgupta, R. (2020). Thermobarometry of CO2-rich, silica-undersaturated melts constrains cratonic lithosphere thinning through time in areas of kimberlitic magmatism. *Earth and Planetary Science Letters*, *550*, 116549. doi: 10.1016/j.epsl.2020.116549

Sun, W., Jiang, J., Dai, L., Hu, H., Wang, M., Qi, Y., & Li, H. (2021). Electrical properties of dry polycrystalline olivine mixed with various chromite contents: Implications for the high conductivity anomalies in subduction zones. *Geoscience Frontiers*, 101178.

Svensen, H., Corfu, F., Polteau, S., Hammer, Ø., & Planke, S. (2012). Rapid magma emplacement in the Karoo Large Igneous Province. *Earth and Planetary Science Letters*, *325-326*, 1–9. doi: 10.1016/j.epsl.2012.01.015

Van Achterbergh, E., Griffin, W. L., & Stiefenhofer, J. (2001). Metasomatism in mantle xenoliths from the Letlhakane kimberlites: Estimation of element fluxes. *Contributions to Mineralogy and Petrology*, *141*(4), 397–414. doi: 10.1007/s004100000236

Van Schijndel, V., Cornell, D. H., Frei, D., Simonsen, S. L., & Whitehouse, M. J. (2014). Crustal evolution of the rehoboth province from archaean to mesoproterozoic times: Insights from the rehoboth basement inlier. *Precambrian Research*, *240*, 22–36. doi: 10.1016/j.precamres.2013.10.014

VanTongeren, J. A. (2017). *Mixing and unmixing in the bushveld complex magma chamber*. Elsevier Inc. doi: 10.1016/B978-0-12-811159-8.00005-6

Wang, D., Karato, S. I., & Jiang, Z. (2013). An experimental study of the influence of graphite on the electrical conductivity of olivine aggregates. *Geophysical Research Letters*, *40*(10), 2028–2032. doi: 10.1002/grl.50471

Wang, D., Mookherjee, M., Xu, Y., & Karato, S. I. (2006). The effect of water on the electrical conductivity of olivine. *Nature*, *443*(7114), 977–980. doi: 10.1038/nature05256

Watson, H. C., Roberts, J. J., & Tyburczy, J. A. (2010). Effect of conductive impurities on electrical conductivity in polycrystalline olivine. *Geophysical Research Letters*, *37*(1), 1–6. doi: 10.1029/2009GL041566

Webb, S. J., Ashwal, L. D., & Cawthorn, R. G. (2011). Continuity between eastern and western Bushveld Complex, South Africa, confirmed by xenoliths from kimberlite. *Contributions to Mineralogy and Petrology*, *162*(1), 101–107. doi: 10.1007/s00410-010-0586-z

Weckmann, U. (2012). Making and Breaking of a Continent: Following the Scent of Geodynamic Imprints on the African Continent Using Electromagnetics. *Surveys in Geophysics*, *33*(1), 107–134. doi: 10.1007/s10712-011-9147-x

White-Gaynor, A. L., Nyblade, A. A., Durrheim, R., Raveloson, R., van der Meijde, M., Fadel, I., ... Sitali, M. (2020). Lithospheric Boundaries and Upper Mantle Structure Beneath Southern Africa Imaged by P and S Wave Velocity Models. *Geochemistry, Geophysics, Geosystems*, *21*(10), 1–20. doi: 10.1029/2020GC008925

Withers, A. C., Bureau, H., Raepsaet, C., & Hirschmann, M. M. (2012). Calibration of infrared spectroscopy by elastic recoil detection analysis of H in synthetic olivine. *Chemical Geology*, *334*, 92–98. doi: 10.1016/j.chemgeo.2012.10.002

Yang, Y., Li, A., & Ritzwoller, M. H. (2008). Crustal and uppermost mantle structure in southern Africa revealed from ambient noise and teleseismic tomography. *Geophysical Journal International*, *174*(1), 235–248. doi: 10.1111/j.1365-246X.2008.03779.x

Youssof, M., Thybo, H., Artemieva, I. M., & Levander, A. (2013). Moho depth and crustal composition in Southern Africa. *Tectonophysics*, *609*, 267–287. doi: 10.1016/j.tecto.2013.09.001

Youssof, M., Thybo, H., Artemieva, I. M., & Levander, A. (2015). Upper mantle structure beneath southern African cratons from seismic finite-frequency P- and S-body wave tomography. *Earth and Planetary Science Letters*, *420*, 174–186. doi: 10.1016/j.epsl.2015.01.034

Zeh, A., Ovtcharova, M., Wilson, A. H., & Schaltegger, U. (2015). The Bushveld Complex was emplaced and cooled in less than one million years - results of zirconology, and geotectonic implications. *Earth and Planetary Science Letters*, *418*, 103–114. doi: 10.1016/j.epsl.2015.02.035

Zeh, A., Wilson, A. H., & Gerdes, A. (2020). Zircon U-Pb-Hf isotope systematics of Transvaal Supergroup – Constraints for the geodynamic evolution of the Kaap-

vaal Craton and its hinterland between 2.65 and 2.06 Ga. *Precambrian Research*, *345*(May), 105760. doi: 10.1016/j.precamres.2020.105760

Zhang, B., & Yoshino, T. (2017, jan). Effect of graphite on the electrical conductivity of the lithospheric mantle. *Geochemistry, Geophysics, Geosystems*, *18*(1), 23–40. doi: 10.1002/2016GC006530

Zhang, B., Yoshino, T., Wu, X., Matsuzaki, T., Shan, S., & Katsura, T. (2012). Electrical conductivity of enstatite as a function of water content: Implications for the electrical structure in the upper mantle. *Earth and Planetary Science Letters*, *357-358*, 11–20.

Zirakparvar, N. A., Mathez, E. A., Scoates, J. S., & Wall, C. J. (2014). Zircon Hf isotope evidence for an enriched mantle source for the Bushveld Igneous Complex. *Contributions to Mineralogy and Petrology*, *168*(3), 1–18. doi: 10.1007/s00410-014-1050-2